Supplementary Information

for

Cortex-wide imaging in naturally behaving mice with 1-gram wireless mesoscopes

Yuanlong Zhang[1,2,9], Angran Li[3,4,9], Lekang Yuan[5,9], Mingrui Wang[6,9], Weihao Zhao[7,9], Zhenbo Wang[1], Boyang Zang[8], Yangxuan Zhou[1], Tao Yu[2], Lin Gao[1], Yu Wu[7], Rongkang Zhu[1], Mengyi Tian[1], Kun Li[1], Jiamin Wu[2]*, Pu Dai[7]* & Qionghai Dai[2]*

[1]IDG/McGovern Institute for Brain Research, Tsinghua-Peking Center for Life Sciences, School of Life Sciences, State Key Laboratory of Membrane Biology, Center for Life Sciences and Artificial Intelligence, Tsinghua University; Beijing, 100084, China.
[2]Beijing Key Laboratory of Cognitive Intelligence, IDG/McGovern Institute for Brain Research, Institute for Brain and Cognitive Sciences, Department of Automation, Tsinghua University; Beijing, 100084, China.
[3]College of Future Information Technology, Fudan University; Shanghai, 200433, China. [4]Zhongguancun Academy; Beijing, 100094, China.
[5]Department of Electrical and Computer Engineering, Princeton University; Princeton, NJ, 08544, USA.
[6]School of Future Technologies, Northeastern University; Shenyang, 110169, China.
[7]Senior Department of Otolaryngology–Head and Neck Surgery, the Sixth Medical Center of Chinese PLA General Hospital, Chinese PLA Medical School; Beijing, 100853, China.
[8]School of Clinical Medicine, Tsinghua University; Beijing, 100084, China.
[9]These authors contributed equally.

*Correspondence: wujiamin@tsinghua.edu.cn (J.W.), daipu301@vip.sina.com (P.D.), qhdai@tsinghua.edu.cn (Q.D.)

This file includes

Supplementary Notes 1 to 5
Supplementary Figures 1 to 19
Supplementary Tables 1 to 4
Supplementary Videos 1 to 16

CONTENT

I. Supplementary Notes

Supplementary Note 1	Curriculum-learning design of Airscope.
Supplementary Note 2	Neuronal signal processing of Airscope.
Supplementary Note 3	Airscope investigates cortical dynamics during 2D and 3D movement.
Supplementary Note 4	Cortical population activity recorded by Airscope during passive and active animal–environment interaction.
Supplementary Note 5	Airscope enables multimodal observation beyond neuronal imaging.

II. Supplementary Figures

Supplementary Figure 1	Aspherical lens system effectively reduces the system length with high performance.
Supplementary Figure 2	Optimized LED illumination design for Airscope to enhance imaging uniformity and efficiency without photobleaching.
Supplementary Figure 3	Filter optimization and PCB design in Airscope.
Supplementary Figure 4	Wireless image transportation and data compression of Airscope.
Supplementary Figure 5	Assembly guide of Airscope.
Supplementary Figure 6	Evaluation of movement agility in mice wearing Airscope.
Supplementary Figure 7	High-resolution 3D skeleton reconstruction of a freely behaving animal wearing Airscope.
Supplementary Figure 8	Field of view and resolution characterization of Airscope.
Supplementary Figure 9	Experimental performance of Airscope compared to a tabletop macroscope.
Supplementary Figure 10	Stable, long-term recordings enabled by Airscope.
Supplementary Figure 11	Hybrid 2p-Airscope recording over different lateral positions in dorsal cortex.

Supplementary Figure 12	Intrinsic signal imaging-based brain region localization pipeline for Airscope.
Supplementary Figure 13	Comparison of multi-animal tracking between SAM2Mice and keypoint-based methods.
Supplementary Figure 14	Dorsal cortical activity patterns that distinguish dominant- and subordinate-animal trials during food and object-play competition.
Supplementary Figure 15	Cortical population activity recorded by Airscope during labyrinth exploration.
Supplementary Figure 16	Cortical responses to vestibular rotational stimulation recorded by Airscope under light and dark conditions.
Supplementary Figure 17	Simultaneous cortex and spinal cord imaging for interrogation of vascular and neuronal dynamics.
Supplementary Figure 18	Simultaneous multimodal imaging using dual Airscopes in freely behaving mice.
Supplementary Figure 19	Neuronal imaging in fully unrestrained animals using the Airscope system.

III. Supplementary Tables

Supplementary Table 1	Overview of current head-mounted miniature microscopes.
Supplementary Table 2	Overview of current wireless devices.
Supplementary Table 3	Parts list of Airscope.
Supplementary Table 4	Component weight of Airscope.

IV. Supplementary Videos

Supplementary Video 1	Overview of the Airscope.

Supplementary Video 2	Assessing Airscope's impact on freely moving behavior.
Supplementary Video 3	Airscope neural recording with high-resolution 3D reconstructed skeletons.
Supplementary Video 4	Robust zero-shot segmentation and identity tracking through SAM2Mice.
Supplementary Video 5	Simultaneous animal group recording with Airscope and multi-animal instance segmentation using SAM2Mice.
Supplementary Video 6	Animal groups wearing Airscope freely exploring large-scale, complex naturalistic environments.
Supplementary Video 7	Neural recording of social hierarchy competition in tube test through Airscope.
Supplementary Video 8	Neural recording of object-play and food competition through Airscope.
Supplementary Video 9	Neural recording of an animal freely exploring a complex maze with Airscope.
Supplementary Video 10	Neural recording of an animal during forced swimming test (FST) with Airscope.
Supplementary Video 11	Neural recording of an animal during tail suspension test (TST) with Airscope.
Supplementary Video 12	Neural recording of an animal during head rotation test with Airscope.
Supplementary Video 13	Simultaneous cortex and spinal cord vascular imaging through Airscope.
Supplementary Video 14	Simultaneous cortex and spinal cord neural imaging through Airscope.
Supplementary Video 15	Integrated recording of neural activity, locomotion, and orofacial dynamics in freely moving mice through Airscope.

Supplementary Video 16	Simultaneous neural and first-person view recording of a freely moving animal with Airscope.

Supplementary Note 1 | Curriculum-learning design of Airscope

We optimized the Airscope framework using a custom curriculum-learning optical design agent, termed LensCopilot. LensCopilot generates a structured, multi-stage optimization curriculum formatted as a JSON file, serving as a comprehensive, static blueprint for the design process (Extended Data Fig. 1a). The curriculum encodes a sequence of optimization stages, each defining monotonically advancing performance targets. Adhering to the core of curriculum learning, this staged approach initiates with conservative parameters, specifically, a narrow field of view and a large F-number, to establish initial stability. The system then progressively transitions toward the final, stringent specifications, effectively mitigating the risk of the optimizer converging on sub-optimal local minima during early iterations.

A critical strategic element encoded within the curriculum is the systematic schedule for releasing degrees of freedom (DoFs). This schedule sequentially unlocks variables, such as surface radii, thicknesses, and aspheric coefficients, at predefined milestones across the optimization stages. Such a domain-informed strategy is imperative for navigating the high-dimensional search space. Optimization typically commences with only low-order aspheric terms (specifically, the A4 coefficient) to establish the fundamental lens geometry and first-order optical properties (Extended Data Fig. 1b). Higher-order terms (e.g., A6 and A8) are progressively activated in subsequent stages to correct higher-order, field-dependent aberrations. Furthermore, the curriculum enforces dynamic manufacturability constraints, including minimum edge thickness and packaging limitations such as total track length (TTL). Finally, it incorporates reusable merit-function templates to guarantee consistent, deterministic evaluation throughout the design trajectory.

A deterministic executor subsequently parses this static curriculum to orchestrate the optimization. For each stage defined in the curriculum, the executor runs a predefined local–Hammer–local (LHL) optimization loop. This protocol initiates with a bounded local optimization phase, utilizing a damped least squares (DLS) algorithm to rapidly converge on the nearest performance plateau. This is followed by a Hammer-style global search, constrained by a pre-allocated iteration budget, designed to escape the local minimum and explore a broader region of the solution space. Each stage concludes with a secondary, constrained local refinement to optimize the solution identified during the global search.

The final optimized optical design of the Airscope is detailed in Extended Data Fig. 1c-k. We note that this design framework is inherently scalable. To see this, utilizing the proposed design pipeline,

we demonstrated two additional variants of Airscope-style optical configurations: 1) Centimeter-scale FOV system, keeping single-cell resolution across the whole FOV (~5 μm, Extended Data Fig. 1l); and 2) Smaller FOV system with high resolution (1 μm, Extended Data Fig. 1m).

Supplementary Note 2 | Neuronal signal processing of Airscope

Analyzing neuronal acquisition of Airscope leverages DeepWonder[1], a deep-learning pipeline for extracting neuronal spatial footprints and calcium activity from scattering-corrupted, widefield one-photon calcium recordings. Calcium imaging movies were processed through a four-stage pipeline consisting of (i) motion-correction and distortion-correction modules that compensated for brain motion and optical aberrations, (ii) a background-rejection network that removed scattering-induced background contamination, (iii) a neuron-segmentation network that identified neuronal spatial footprints from the cleaned frames, and (iv) a temporal trace-extraction module that generated demixed neuronal activity traces from the segmented ROIs.

Stage 1: Pre-processing of experimental recordings (motion correction, distortion correction and ROI cropping). Raw one-photon calcium imaging frames were motion-corrected using the NoRMCorre[2] registration algorithm. The maximum allowed shift was set to 100 pixels in both axes, with 96-pixel patch strides, 48-pixel overlaps. To reduce memory usage for long recordings, each recording was divided into temporal chunks (1000 frames as default), and a registration template was estimated and propagated across chunks to maintain consistency over the full movie. Both rigid and piecewise non-rigid registration were performed to compensate for global brain motion and local tissue deformation.

After motion correction, optical field distortion was corrected using a pre-calibrated distortion map of the Airscope system (Extended Data Fig. 4c). The corrected field of view was then cropped to the calcium imaging region of interest.

Stage 2: background rejection (RB-Net). The preprocessed movie was then passed through a trained RB-Net, following the DeepWonder. RB-Net was a 3D U-Net with three encoder/decoder convolutional blocks and ~4 million parameters. This network separated neuronal fluorescence from background contamination caused by out-of-focus fluorescence, neuropil signals, tissue scattering and hemodynamic contamination. The network output contained a background component and a neuron-enriched component. Background-suppressed movie was used for subsequent segmentation and trace extraction.

Stage 3: neuron segmentation (NS-Net). Neurons were segmented from the background-suppressed movie using a spatiotemporal segmentation procedure adapted from the DeepWonder NS-Net post-processing framework. NS-Net shared the 3D U-Net backbone but was much lighter (~0.9 M parameters): the full 3×3×3 convolutions were factorised into a 1×1×3 temporal filter

combined with a 3×3×1 spatial filter, and a final max-pooling layer compressed the temporal axis so the network output a single 2D binary segmentation mask per input clip.

Stage 4 — Candidate refinement and signal extraction. NS-Net masks across all frames were grouped by spatio-temporal connectivity; spatially overlapping but temporally distinct components were treated as separate neuronal candidates. Each candidate was then filtered by morphology — area (threshold 25 μm²) and roundness $\theta = 4\pi s/p^2$ (where s and p were area and perimeter). Candidates with $\theta \geq 0.8$ entered the "good" list; those with lower roundness (likely fused somata) entered the "bad" list. Further judgement included:

- Neuronal diameter ≥ 10 μm.
- Elliptical roundness (major/minor axis) ≤ 3.
- Mask occupancy ≥ 50%, where occupancy = (mask pixels inside bounding box) / (bounding-box width × bounding-box height)
- Temporal consistency across ≥ 5 consecutive frames
- Probability-map confidence through DeepWonder network ≥ 0.5
- Centroid not located within the vessel or outside-FOV exclusion zone

For accepted neurons, the spatial footprint was stored as a binary ROI mask. The calcium trace of each neuron was extracted directly from the RB-Net-cleaned movie. For "good" neurons, temporal traces were read directly from exclusive (non-overlapping) pixels of the RB-Net-cleaned movie, exploiting the fact that the cleaned movie contained negligible inter-neuron crosstalk. For "bad" neurons, each candidate was re-initialized using a greedy ROI method, as in CNMF-E[3], and then refined by local non-negative matrix factorization by solving:

$$\min_{A,C\geq 0} \frac{1}{2} \| Y - AC \|_F^2 + \alpha_A \| A \|_1 + \alpha_C \| C \|_1$$

where Y denotes the local background-suppressed movie, A denotes the spatial footprints, and C denotes the temporal calcium activity. The optimization was solved using hierarchical alternating least squares. Components with high temporal correlation and spatial overlap were subsequently merged. NS-Net + local NMF reliably demixed neurons separated by as little as 0.3 neuron diameters (temporal similarity > 0.9, spatial similarity > 0.85). The final outputs were the spatial footprints, centroid coordinates and temporal calcium traces for all retained neurons.

Neuron counts for every experimental panel

Animal ID	Figure panel	Verified neurons
14_#autism	Fig. 2k,	8583
8#	Fig. 2l-n, Supplementary Fig. 9d-h,	4560
1#_spine	Fig. 6e-g ,	4253
3_new#	Fig. 3d, Fig. 3h, Fig. 3i, Extended Data Fig. 7d-e,	5,944
7#	Fig. 3g, Fig. 5e-f, Fig. 5h-i, Extended Data Fig. 9h, Extended Data Fig. 9m, Extended Data Fig. 10c-d, Extended Data Fig. 10f-g, Extended Data Fig. 10k-l, Extended Data Fig. 7d-e, Supplementary Fig. 15a-b, Supplementary Fig. 15d-e,	7133
20#	Fig. 3i, Fig. 5e-f,	5,823
5_new#	Fig. 3i, Extended Data Fig. 7d-e,	7,709
swim#	Extended Data Fig. 9a-g,	2,657
16#	Fig. 5e-f, Fig. 5i, Extended Data Fig. 9h, Extended Data Fig. 9k-m, Supplementary Fig. 15d-e,	3778
6#	Extended Data Fig. 9h, Extended Data Fig. 9m,	2,643
80#	Extended Data Fig. 9h, Extended Data Fig. 9m, Extended Data Fig. 7d-e,	1,736
6_new#	Extended Data Fig. 7d-e,	5,242
1#_cage_3	Fig. 4b, Fig. 4f-m, Fig. 4p-r, Extended Data Fig. 8, Supplementary Fig. 14,	5,609
2#_cage_3	Fig. 4b, Fig. 4f-m, Fig. 4p-r, Extended Data Fig. 8, Supplementary Fig. 14,	5,331
3#_cage_3	Fig. 4b, Fig. 4f-m, Extended Data Fig. 8,	3714
4#_cage_3	Fig. 4b, Fig. 4f-m, Extended Data Fig. 8,	3,893
1#_cage_2	Fig. 4b, Fig. 4f-m, Fig. 4p-r, Extended Data Fig. 8,	4,574
2#_cage_2	Fig. 4b, Fig. 4f-m, Extended Data Fig. 8,	1,834

3#_cage_2	Fig. 4b, Fig. 4f-m, Fig. 4p-r, Extended Data Fig. 8, Supplementary Fig. 14,	6,755
4#_cage_2	Fig. 4b, Fig. 4f-m, Extended Data Fig. 8, Supplementary Fig. 14,	4,962
1#_cage_1	Fig. 4b, Fig. 4c-e, Supplementary Fig. 14,	3812
2#_cage_1	Fig. 4b,	4,573
3#_cage_1	Fig. 4b,	3,326
4#_cage_1	Fig. 4b, Fig. 4c-e, Supplementary Fig. 14,	5807
1#_3D_terrain	Extended Data Fig. 3u-v,	3921
2#_3D_terrain	Extended Data Fig. 3u-v,	3944
3#_3D_terrain	Extended Data Fig. 3u-v,	3143

Supplementary Note 3 | Airscope investigates cortical dynamics during 2D and 3D movement

Rodents are highly agile in three dimensions. To compare locomotion and neuronal activity between tethered and untethered configurations, we performed paired recordings in the same animals and cortical regions under both wired (power and data) and fully wireless operation, and tested each animal with both configurations in 2D and 3D environments.

In the first scenario, we compared locomotor behavior in the same animals wearing either a wireless Airscope or a cable-tethered Airscope in a 40 cm × 40 cm open field (Extended Data Fig. 3a). The tethered configuration used a Cooner wire (CW8251), consistent with the head-mounted weight used in Extended Data Fig. 2 and commonly adopted in tethered miniature microscopes such as Miniscope V3[4] and Miniscope V4[5]. In this planar open-field arena (40 × 40 cm), the two configurations exhibited comparable locomotor behavior, including cumulative distance, speed distribution, total distance traveled, and 75th percentile speed (Extended Data Fig. 3d-g). These results indicate that, in planar movement, tethering of a miniscope in animal's head will not cause large differences compared to fully untethered mode.

In the second scenario, animals were recorded in a 60 × 60 cm arena containing hexagonal pillars that form a heterogeneous 3D terrain (Extended Data Fig. 3h). An RGB-D camera was used to capture vertical motion, and SAM2Mice enabled precise spatiotemporal detection of height-change events, including climbing and descending transitions. In contrast to the planar condition, tethered animals in the 3D environment exhibited altered locomotor patterns, including reduced cumulative absolute exploration distance and lower locomotor speed (Extended Data Fig. 3k-n). The total spatial area explored was also markedly reduced (Extended Data Fig. 3j). This reduction was accompanied by a decreased capacity for vertical transitions, as reflected by a lower frequency of height-change events in tethered animals compared to the untethered condition (Extended Data Fig. 3q-r).

We subsequently investigated whether these behavioral discrepancies manifested as measurably distinct dorsal cortical activity patterns. To address this, we longitudinally registered neuronal coordinates within the same animals across tethered and untethered conditions (Extended Data Fig. 3s). Our analysis was specifically time-locked to height-change events, which were first classified into two behavioral categories, ascend and descend, based on the direction of vertical displacement. At the single-neuron level, we identified individual neurons that were tuned to ascend and descend behaviors in both the untethered and tethered conditions (Extended Data Fig. 3t).

To visualize population-level neural dynamics, we projected trial-averaged activity associated with ascending and descending events into a shared low-dimensional state space using PCA (Methods)[6]. Neural trajectories were constructed by connecting the projected population activity across time bins for each behavioral condition. We discovered that neural trajectories corresponding to both descending (higher to lower platform) and ascending (lower to higher platform) behaviors exhibited characteristic clockwise (CW) rotational dynamics. Notably, both conditions drove a segregation of neural activity subspaces even prior to the onset of the height change, indicating the presence of separable brain states preceding trial initiation (Extended Data Fig. 3u). Furthermore, animals in the tethered condition displayed elongated neural trajectories compared to their untethered counterparts (Extended Data Fig. 3u).

To test whether dorsal cortical populations encode ascending and descending movements, we trained a support vector machine (SVM) classifier on single-trial neural activity. Decoding accuracy increased around the onset of height change in both conditions, peaking several frames after the transition (Extended Data Fig. 3v). However, cross-condition transfer was minimal: decoders trained on wired recordings performed at near-chance levels when tested on Airscope data, and similarly, decoders trained on Airscope recordings showed near-chance performance on wired data (Extended Data Fig. 3v). These results indicate that cortical representations of vertical movement are largely condition-specific, with limited generalization across tethered and untethered configurations.

Supplementary Note 4 | Cortical population activity recorded by Airscope during passive and active animal–environment interaction

Airscope enables imaging during natural, diverse behaviors without restricting animals' movement repertoire. As a first demonstration, we used Airscope to record cortical activity during two widely used rodent assays—the forced-swimming test (FST) and the tail-suspension test (TST)[7]—in which behavioral phases such as struggling, swimming, floating, and quiescence have historically been quantified without concurrent cortex-wide imaging, because conventional microscopy is unsuitable for vigorous swimming and head-mounted devices have been limited by weight, waterproofing, and motion artifacts.

Airscope precisely fills this niche. Its lightweight, untethered design minimally perturbs freely swimming and suspended animals (Extended Data Fig. 9h and Supplementary Video 10). For water resistance, we encased the device in a plastic wrapper (Methods). As in standard FST, animals initially swam on entry, then struggled; over time stamina waned, producing floating and eventual exhaustion, occasionally with choking (Extended Data Fig. 9b). A similar stamina-dependent transition from struggling to giving up appeared in the TST, which included more bouts than the FST (Extended Data Fig. 9i).

Aligning cortex-wide activity to behavioral transitions, we observed activity modulations at the swimming to struggling transition (n = 13 trials) and the struggling to floating transition (n = 9 trials), with region-specific time courses (Extended Data Fig. 9d). To quantify how much information about behavioral phase is carried by cortical activity, we trained a compact CNN classifier to read out phase from population activity (Extended Data Fig. 9e). Five-fold cross-validation yielded an AUC of 0.957 $\pm$ 0.02 (n = 5 folds, mean $\pm$ SD; Extended Data Fig. 9f), with struggling decoded most reliably (precision 0.959 ± 0.015, recall 0.935 ± 0.038, F1 0.946 ± 0.015) and swimming next (precision 0.839 ± 0.079, recall 0.885 ± 0.073, F1 0.856 ± 0.042). Decoding performance for floating was lower and is likely limited by the smaller number of floating frames in the dataset (precision 0.647 ± 0.253, recall 0.576 ± 0.206, F1 0.538 ± 0.117; Extended Data Fig. 9g). These analyses indicate that FST behavioral phase is decodable from dorsal-cortical population activity.

In the TST (Extended Data Fig. 9h, i and Supplementary Video 11), transitions between struggling and quiescence occurred more frequently than in the FST. Across bouts, the activity of widely distributed neurons was positively and negatively correlated with struggling, and these correlations

extended beyond motor cortex (Extended Data Fig. 9k). A subset of neurons showed activity changes that statistically preceded struggling onset; these lead-time cells were distributed across cortex and were denser in primary motor cortex (MOp; Extended Data Fig. 9l). Using an SVM trained on cortical activity, active and passive states were decoded with accuracy above chance (0.832 ± 0.055 across $n = 4$ animals; $p = 0.0209$, two-sided Wilcoxon rank-sum), and the two states occupied separable regions of a t-SNE embedding[8] of population activity (Extended Data Fig. 9m).

We next applied Airscope to animals undergoing complex passive motion, with mice standing on a rapidly rotating stage (Supplementary Fig. 16a). Tethered microscopes, even with commutators, can suffer from cable twisting and torque artifacts during rotation, whereas the untethered Airscope provided uninterrupted recording across the same protocol (Supplementary Video 12). Cortical activity covaried with head orientation across many regions (Supplementary Fig. 16e), and a subset of neurons showed activity that covaried with angular head velocity; these velocity-correlated neurons were distributed across the imaged cortical area (Supplementary Fig. 16d–f). Comparing light and dark conditions, the spatial distribution of velocity-correlated neurons and the directed predictive (Granger-causality) networks computed from population activity differed between conditions (Supplementary Fig. 16g, h and Methods). Decoding rotation speed from neurons that were active in the light produced lower error than decoding from the matched population in the dark (Supplementary Fig. 16i). This observation is consistent with previous reports that visual input increases the discriminability of angular self-motion signals[9].

Supplementary Note 5 | Airscope enables multimodal observation beyond neuronal imaging

Airscope is a scalable device that can record facial expressions and environmental context alongside neuronal activity. We first used it to ask how orofacial behaviors covary with distributed cortical activity, a question of growing interest[10].

While we acknowledge several pioneering studies, including Meyer et al. (2018)[11], who established lightweight head-mounted camera monitoring in freely moving mice, and Parker et al. (2022)[12], who combined eye and head measurements with visual input from the mouse's perspective, progress has been limited because existing tools rarely capture cortical activity together with fine orofacial dynamics in freely behaving animals. We therefore built a compact dual-Airscope, equipping one of the units with a custom wide-field lens (120° FOV, 0.1 g) to image full-face expressions in mice alongside the cortical imaging (Extended Data Fig. 10a, Supplementary Fig. 18a and Supplementary Video 15). This wearable configuration surpasses tabletop microscope–camera systems in size and capability. Animals freely explored while wearing the device, displaying diverse pupil dynamics and facial expressions (Extended Data Fig. 10a).

Consistent with prior research, we find unsupervised clustering of pairwise frame similarity revealed no distinct clusters, indicating no consistent changes in facial expressions during spontaneous behavior (Supplementary Fig. 18b). A close look revealed that during freely exploration, the animal exhibits rich eye movement and some grooming behavior (Extended Data Fig. 10c). The activity of widely distributed dorsal-cortical neurons was correlated to both behaviors (Extended Data Fig. 10c), but with diverse distributions (Extended Data Fig. 10d).

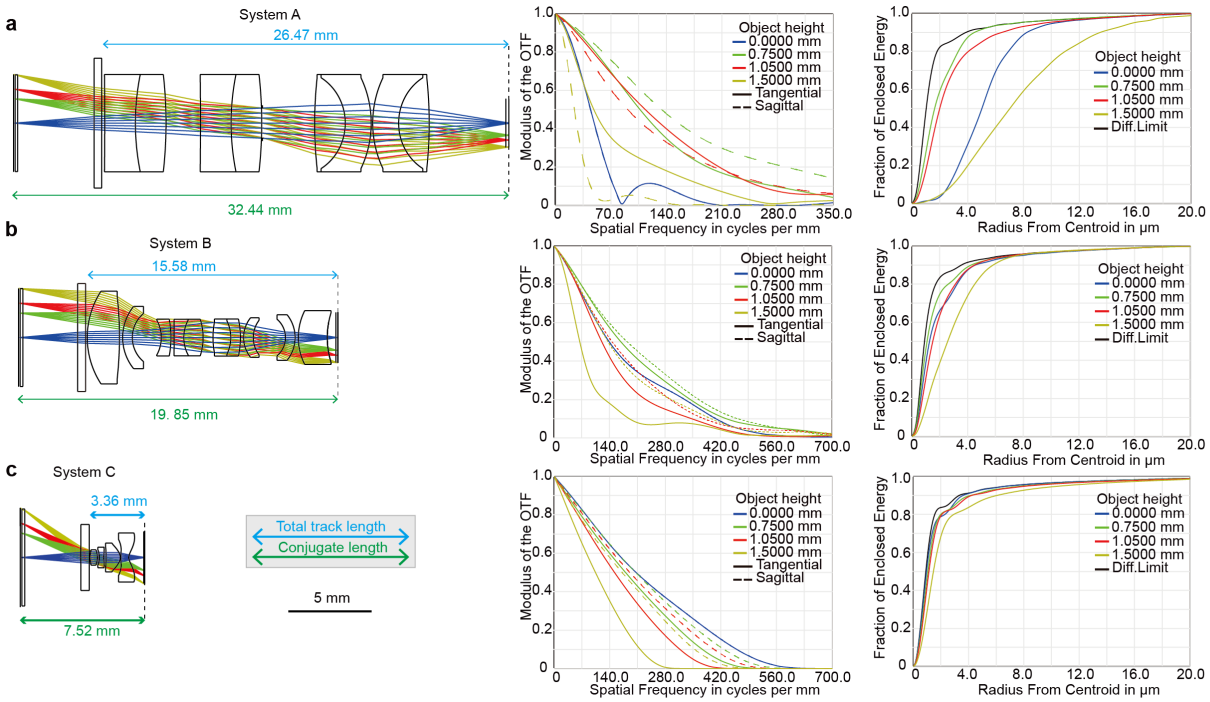
To quantify the predictive relationship between orofacial behavior and dorsal cortical activity, we trained a deep neural network to predict neural signals from behavioral features[13] (Extended Data Fig. 10e). The model employs a one-dimensional convolutional layer with temporal filters to extract spatiotemporal patterns from orofacial key-point trajectories, followed by fully connected layers for activity prediction (Methods). Single-trial activity of thousands of simultaneously recorded neurons was predictable from facial features, with close agreement between observed and predicted raster plots (Extended Data Fig. 10g), and the neurons whose activity was well predicted by facial features were spatially spread across the imaged cortical area (Extended Data Fig. 10f and Methods). We interpret this as evidence that facial behavior is statistically coupled to dorsal-cortical activity at single-neuron resolution.

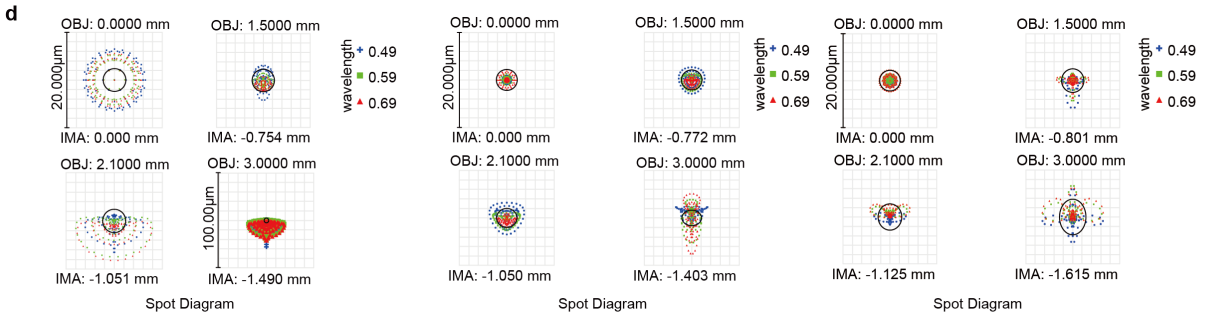
We next leveraged Airscope to monitor neural activity and external context simultaneously, demonstrating its applicability to questions of visual processing in awake, freely behaving mice (Supplementary Video 16). Inspired by Holmgren et al. (2021)[14], who reconstructed the visual field from eye tracking and geometric modeling, we modified the dual system, equipping one of the units with a 2.6-mm lens, approximating the mouse focal length[15], to capture the scene from the animal's perspective (Extended Data Fig. 10h).

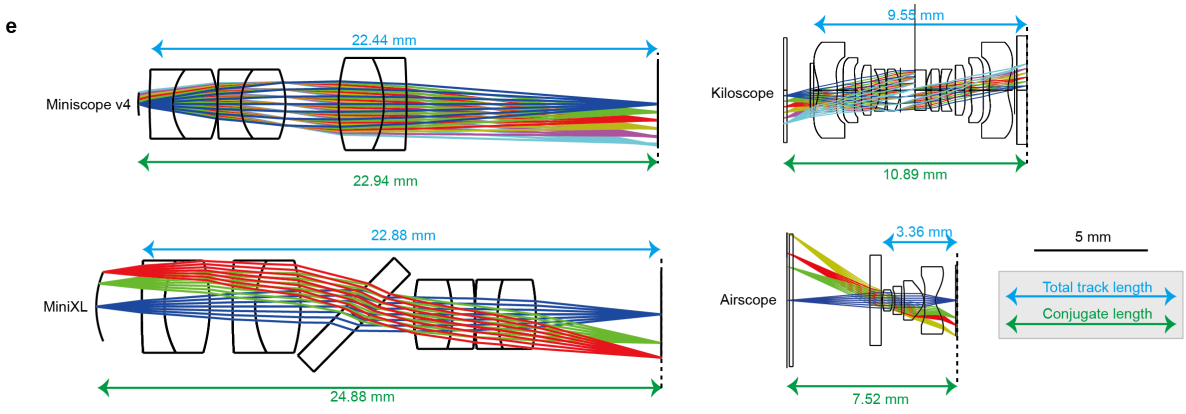
Mice explored a circular arena with walls painted in gratings of multiple orientations, adapting the standard static-grating assay used under head fixation (Supplementary Fig. 18c). In free movement, the visual input stream was richer than in the head-fixed paradigm: animals could sweep across all four gratings in a single motion, or dwell on a single grating within the same time window (Extended Data Fig. 10h and Supplementary Fig. 18d). Neurons whose orientation preference had been defined under head fixation showed activity that covaried with the corresponding gratings during free exploration (Extended Data Fig. 10i).

To characterize cortex-wide visually evoked activity, we co-embedded visual stream and neural data in a shared low-dimensional manifold. We extracted frame-wise embeddings from the visual stream using a pretrained DINO encoder[16], aligned them with simultaneous Airscope recordings, and applied CEBRA[17] to learn joint latent representations (Extended Data Fig. 10j). The resulting CEBRA-Behavior space showed clearly segregated clusters corresponding to distinct stimuli (Extended Data Fig. 10k and Supplementary Fig. 18e). As expected, neurons in visual cortex most effectively predicted visual input (Extended Data Fig. 10l). Interestingly, joint training across multiple visual cortical regions does not improve classification performance (Supplementary Fig. 18g).

Supplementary Figures 1-19

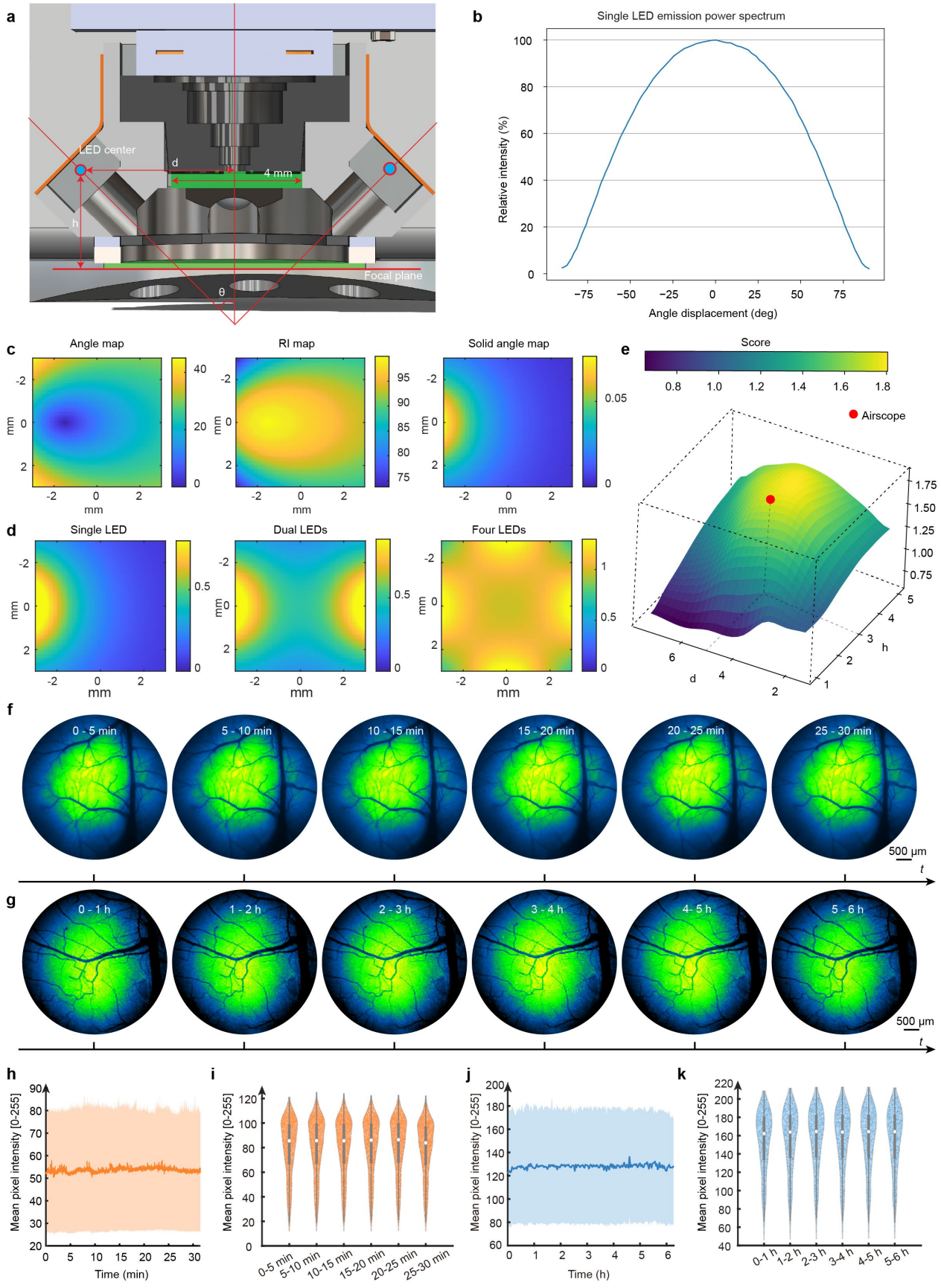






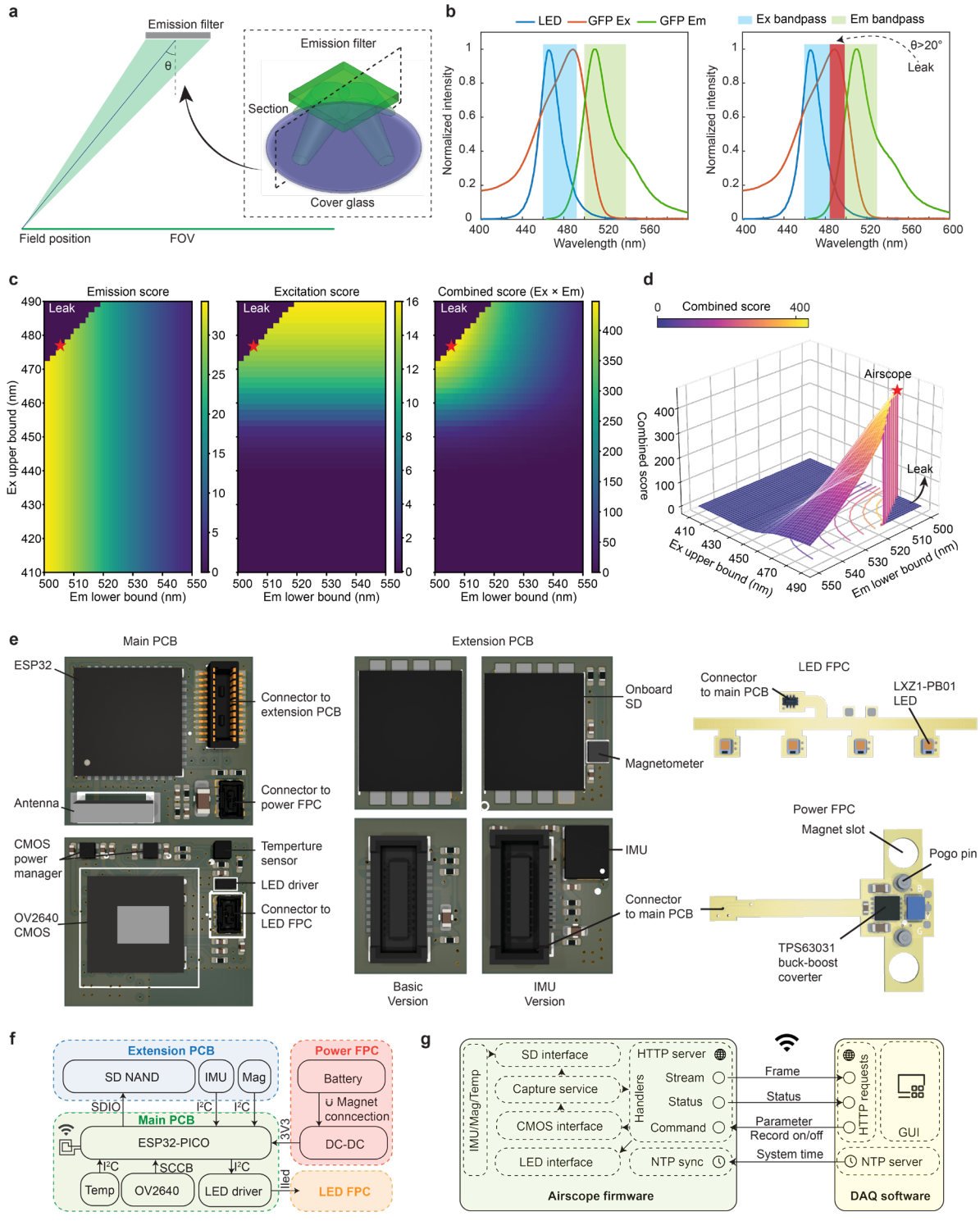
Supplementary Fig. 1 | Aspherical lens system effectively reduces the system length with high performance.

a, Optical layout of the modified multi-achromat system (System A), adjusted to match the Airscope's field of view, magnification, and numerical aperture. Corresponding modulation transfer function (MTF) curves and fraction of enclosed energy shown on the right. Total track length: 26.47 mm. **b,** as in **a** but employing an advanced meniscus lens; total track length: 15.58 mm (System B). **c,** Optical design of the Airscope; total track length: 3.36 mm (System C). Blue arrows indicate the total track length (Methods), and green arrows indicate the conjugate length (Methods). **d,** Comparison of spot diagrams among the three systems (A–C, left to right). **e,** Total track length comparison among Miniscope V4, MiniXL, Kiloscope and Airscope. Scale bars: 5 mm (**a**, **b**, **c** and **e**).


a
LED center
d
4 mm
h
Focal plane
θ
b
Single LED emission power spectrum
Relative intensity (%)
Angle displacement (deg)
c
Angle map
RI map
Solid angle map
mm
d
Single LED
Dual LEDs
Four LEDs
e
Score
Airscope
d
h
f
0 - 5 min
5 - 10 min
10 - 15 min
15 - 20 min
20 - 25 min
25 - 30 min
500 µm
t
g
0 - 1 h
1 - 2 h
2 - 3 h
3 - 4 h
4- 5 h
5 - 6 h
500 µm
t
h
Mean pixel intensity [0-255]
Time (min)
i
Mean pixel intensity [0-255]
0-5 min
5-10 min
10-15 min
15-20 min
20-25 min
25-30 min
j
Mean pixel intensity [0-255]
Time (h)
k
Mean pixel intensity [0-255]
0-1 h
1-2 h
2-3 h
3-4 h
4-5 h
5-6 h

Supplementary Fig. 2 | Optimized LED illumination design for Airscope to enhance imaging uniformity and efficiency without photobleaching.

a, Simulation framework for optimizing LED illumination geometry. Three parameters were varied: (1) the LED angle θ relative to the collection lens optical axis, (2) LED lateral separation distance d, and (3) vertical distance h from LED to the focal plane. A multivariable optimization was performed to maximize both illumination uniformity and efficiency over a Φ 6 mm field of view (FOV). **b,** Angular emission profile of a single LED, showing relative intensity as a function of angular displacement. **c,** Simulated angle map, angular emission relative intensity (RI) map and solid angle map from single LED. **d,** Focal plane illumination intensity expressed as the product of its angular emission profile and corresponding solid angle distribution when single, dual and four LEDs are used. **e,** Three-dimensional visualization of the optimization process for illumination performance at a fixed incident angle of θ = 45°. The composite score was calculated as the sum of three normalized metrics — illumination uniformity, minimum intensity, and mean intensity. Optimal illumination was achieved at approximately d = 5 mm, and h = 3 mm. The red dot indicates the current Airscope configuration. **f,** Mean intensity projection of neuronal imaging within six time segments across a 30-minute recording. **g,** Mean intensity projection of microglia imaging within six time segments across a 6-hour recording. **h,** Pixel intensities across entire FOV from 30-minute recordings of neurons. Thick line: Mean; shaded region: ± SD. **i,** Violin plots of pixel intensities within segmented neuron regions across 30-minute recordings, binned in 5-minute intervals. White circle: median; grey bar: interquartile range; thin lines: upper and lower adjacent values; violins: kernel density estimates; dots: data points of individual cells. **j,** Pixel intensities across entire FOV from 6-hour recordings of microglia in cortex; symbols are the same as in **h**. **k**, Violin plots of pixel intensities within detected microglia across 6-hour recordings, binned in 1 hour; symbols are the same as in **i**. Scale bar: 500 μm (**f** and **g**).

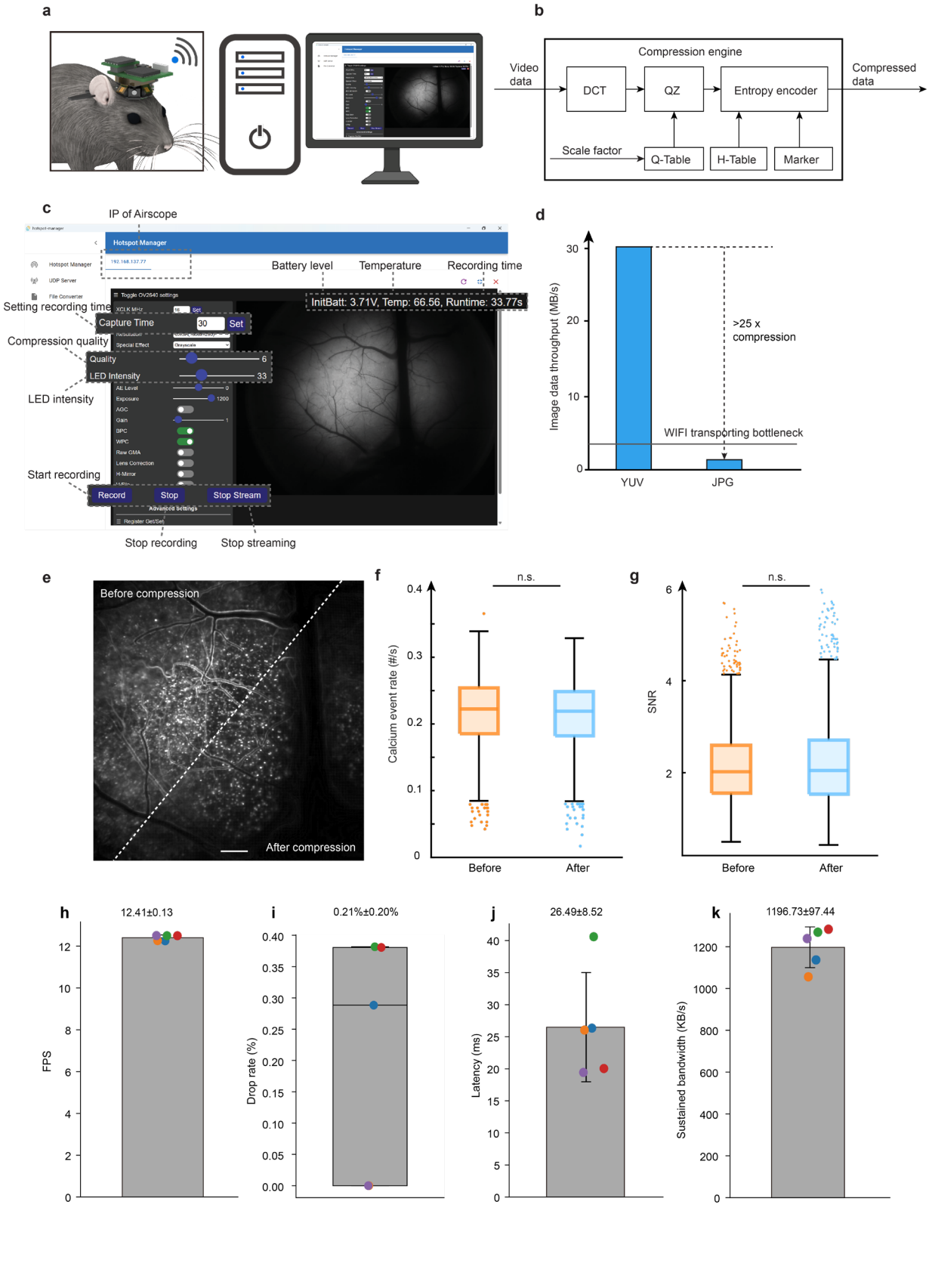


Supplementary Fig. 3 | Filter optimization and PCB design in Airscope.

a, Illustration of field position-dependent incident angle to the emission filter across the field of view. **b,** Spectral profiles of the excitation LED (blue), GFP absorption (red), and GFP emission (green) across wavelengths. Right, angle-dependent blue shift of the emission filter's bandpass,

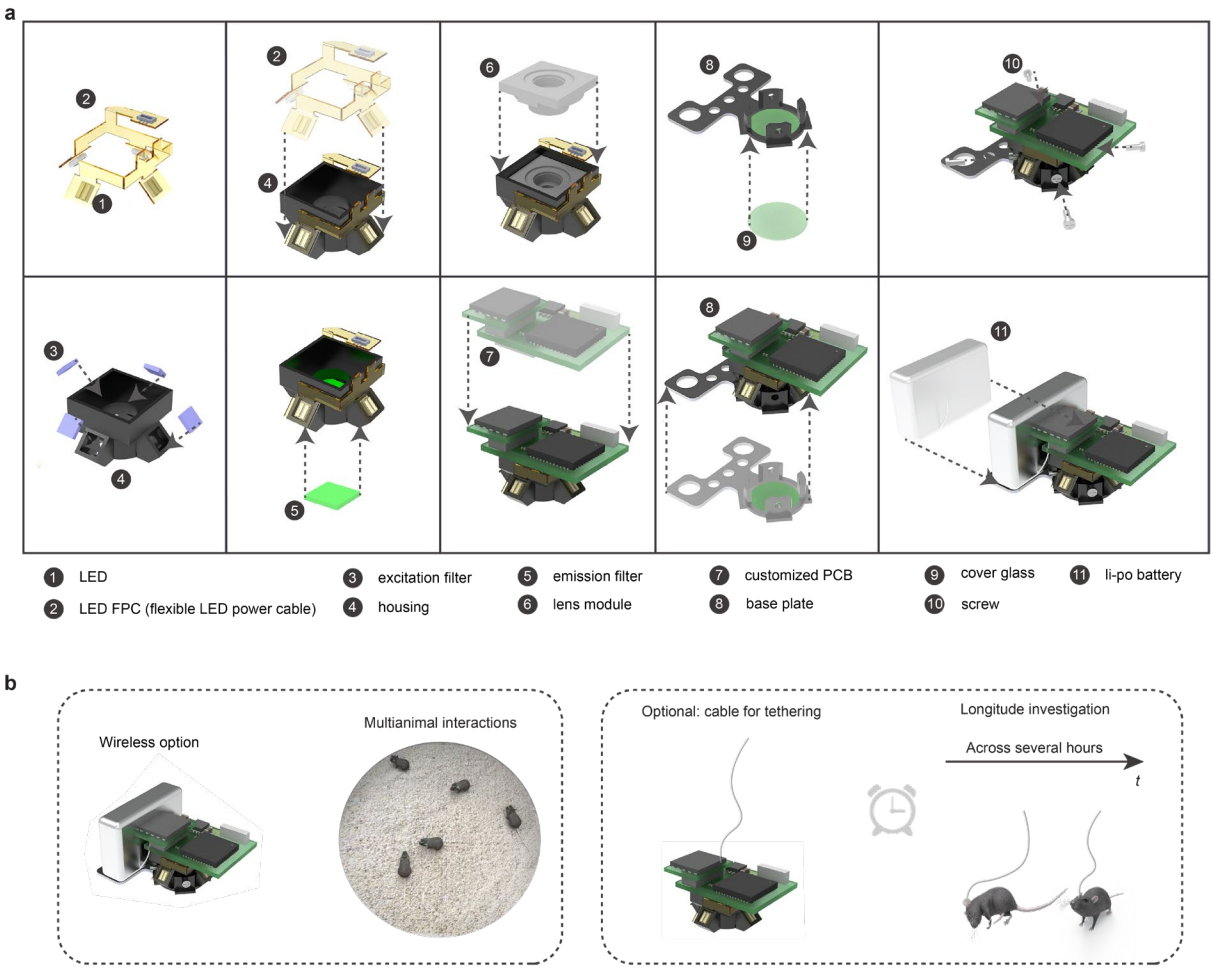
which may induce spectral leakage at high incident angles represented by the red shaded area. **c,** Computational evaluation of emission score, excitation score, and combined optical performance score as functions of the excitation filter cutoff (Ex upper bound) and emission filter cutoff (Em lower bound). Optimal cutoff wavelength choice was identified by a red star. **d,** Grid search results of filter optimization visualized in 3D. Warmer colors mean higher scores (product of excitation efficiency and collection efficiency). Optimal cutoff wavelength choice was identified by a red star. **e,** 3D-rendered custom-designed main PCB (left), extension PCB with top and bottom views (center), and FPC modules for LED and power management (right). The main PCB integrates an OV2640 CMOS image sensor, clock oscillator, Wi-Fi antenna, LED driver for excitation LEDs, temperature sensor, and a power sequencer that regulates sensor voltage supply and sequencing. The extension PCB features an onboard SD card slot, inertial measurement unit (IMU) for detecting linear and angular head accelerations, and a magnetometer for head orientation tracking. The LED FPC includes four LXZ1-PB01 LEDs for illumination. The power FPC incorporates embedded magnets and pogo pins enabling a "snap-and-go" connection, along with a TPS63031 buck-boost converter for efficient power regulation. **f,** Modular electronics architecture of the Airscope. The main PCB (green) is built around an ESP32 system-on-chip that handles Wi-Fi telemetry, acquires images from an OV2640 CMOS sensor via the serial camera control bus (SCCB), polls an on-board temperature sensor, and programs a constant-current LED driver over I^2C. A plug-in extension PCB (blue) adds high-speed SD-NAND mass storage through an SDIO interface together with an inertial-measurement unit (IMU) and three-axis magnetometer, both addressed on the same I^2C bus. Power is delivered by a flexible power cable (red) that couples a Li-polymer battery to a DC–DC converter, providing a regulated 3.3 V rail to the main board. Illumination current is routed through a dedicated LED FPC (orange) to minimize electromagnetic interference with sensitive sensor lines. Dashed outlines denote the physically separable sub-assemblies. **g,** Network-synchronized firmware-to-host workflow of Airscope. The on-device firmware layers (left, green) marshal sensor inputs (IMU, magnetometer, temperature), camera frames, and LED-driver commands through modular service blocks that feed an embedded HTTP server. Dedicated handlers expose three endpoints—Stream for continuous frame delivery, Status for health polling, and Command for real-time parameter updates and record-toggle control—while an NTP client maintains system-time alignment with the host. A desktop data-acquisition (DAQ) suite (right, yellow) issues REST-style HTTP requests, displays incoming video in a graphical user interface, and serves as

the local NTP source. All traffic traverses a bidirectional Wi-Fi link, eliminating physical tethers while preserving deterministic timing and closed-loop control.


a
b
Compression engine
Video data
DCT
QZ
Entropy encoder
Compressed data
Scale factor
Q-Table
H-Table
Marker
c
IP of Airscope
Hotspot Manager
Battery level
Temperature
Recording time
InitBatt: 3.71V, Temp: 66.56, Runtime: 33.77s
Setting recording time
Capture Time
30
Set
Compression quality
Quality
6
LED Intensity
33
LED intensity
Start recording
Record
Stop
Stop Stream
Stop recording
Stop streaming
d
Image data throughput (MB/s)
>25 x compression
WIFI transporting bottleneck
YUV
JPG
e
Before compression
After compression
f
n.s.
Calcium event rate (#/s)
Before
After
g
n.s.
SNR
Before
After
h
12.41±0.13
FPS
i
0.21%±0.20%
Drop rate (%)
j
26.49±8.52
Latency (ms)
k
1196.73±97.44
Sustained bandwidth (KB/s)

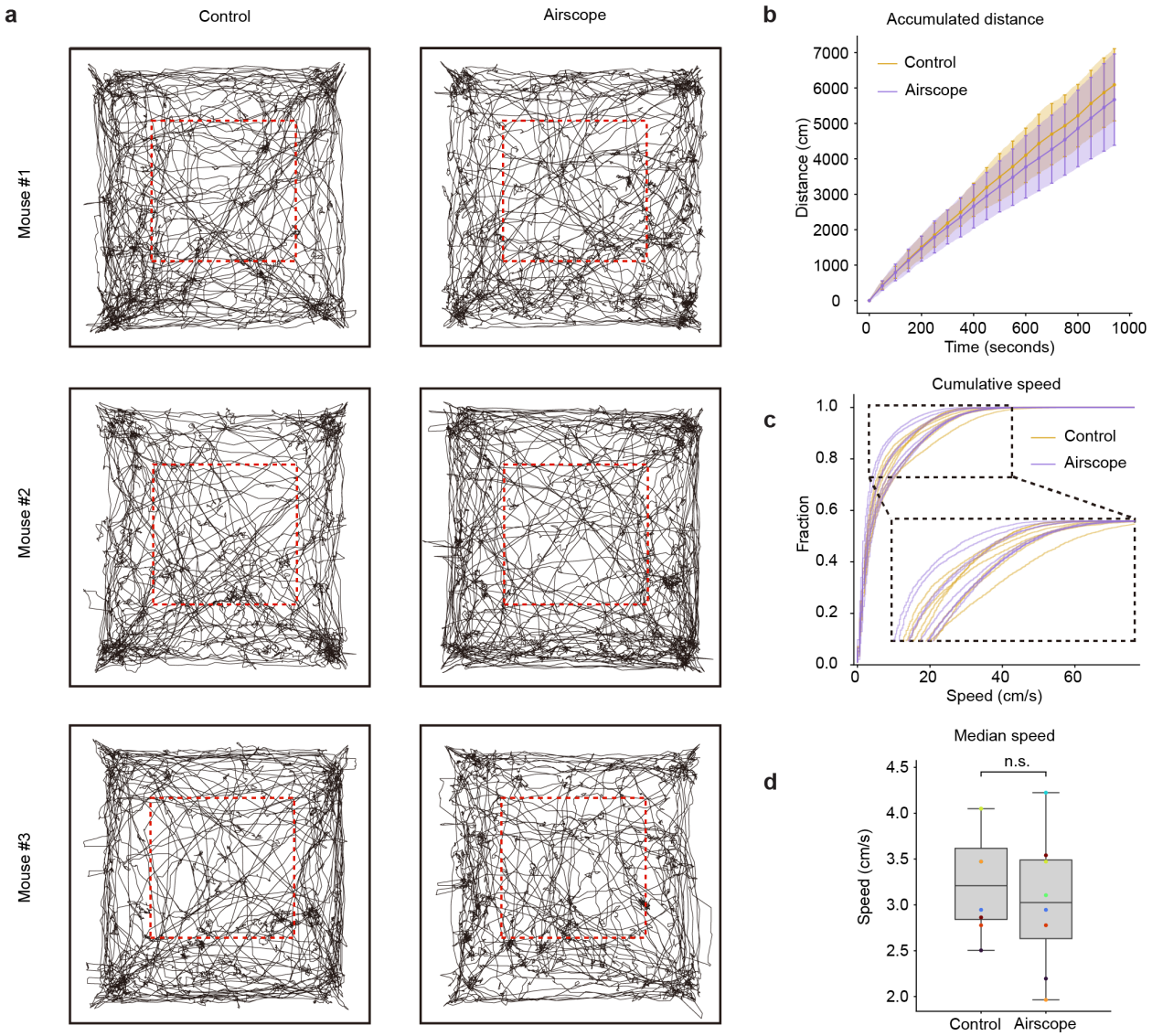
Supplementary Fig. 4 | Wireless image transportation and data compression of Airscope.

a, Schematics of wireless data transportation of Airscope. **b,** Airscope incorporates an on-chip data compression pipeline to overcome the limitations of wireless transmission bandwidth. Instead of directly transmitting raw images from the CMOS sensor, the data undergo three key processing stages: Discrete Cosine Transform (DCT), Quantization (QZ), and Entropy Encoding. The DCT converts spatial image data into the frequency domain, concentrating essential visual information into low-frequency components. Quantization then reduces data volume by discarding high-frequency components that are less perceptually significant, introducing controlled compression loss. Finally, entropy encoding further compresses the data by assigning shorter codes to more frequently occurring values. **c,** A customized image acquisition GUI was developed specifically for Airscope, enabling researchers to remotely preview and control imaging via a local laptop. The interface allows real-time adjustment of acquisition parameters, including exposure time and LED brightness, and provides seamless initiation of image recording. **d,** Image data throughput before (~30 MB s^{-1}) and after (~1 MB s^{-1}) compression. Compression reduces the throughput more than 25-fold, below the Wi-Fi transmission limit of the microcontroller (~3.5 MB s^{-1}), which uncompressed data exceed. **e,** Comparison of standard deviation projection of cortical imaging results acquired before and after compression. **f,** Comparison of calcium event rate of neuronal populations before (orange) and after compression (blue). No significant difference (n.s.) was observed ($p = 0.080$, two-sided Wilcoxon rank-sum test, 2427 data points from the uncompressed data, 2215 data points from the compressed data). Central line inside the box: Median. Box: Interquartile range. Whiskers: Maximum and minimum. Outliers: Individual data points. **g,** Comparison of signal-to-noise ratio (SNR) of neuronal populations before (orange) and after compression (blue). No significant difference was observed ($p = 0.085$, two-sided Wilcoxon rank-sum test, 2427 data points from the uncompressed data, 2215 data points from the compressed data). Central line inside the box: Median. Box: interquartile range. Whiskers: Maximum and minimum. Outliers: Individual data points. **h-k,** Airscope wireless performance verification. FPS (**h**); Dropout rate (**i**); End-to-end latency (**j**); Sustained bandwidth (**k**). Values are presented as mean ± SD from five Airscopes, with all devices operating simultaneously on the same Wi-Fi access point. Scale bar: 500 μm (**e**).



Supplementary Fig. 5 | Assembly guide of Airscope.

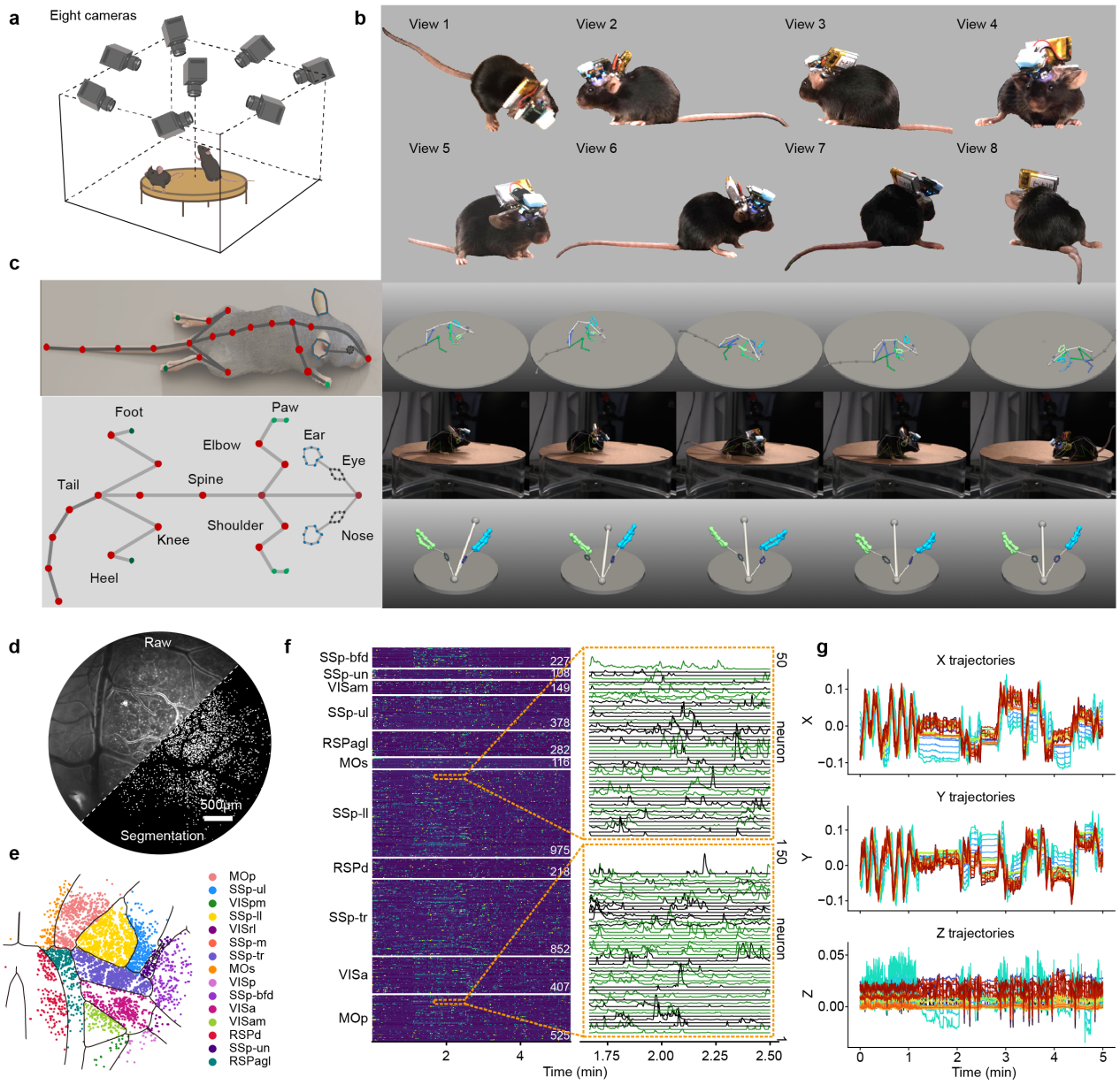
a, Stepwise assembly of the Airscope with battery charging. The flexible printed circuit-mounted (FPC) LED, along with the excitation filter, is first wrapped and secured within the 3D-printed housing. Subsequently, the aspherical lens module and emission filter are inserted. The full PCB is then installed, completing the core body assembly. A diced coverglass is adhered to the base plate and affixed to the mouse skull. The assembled Airscope is inserted and fixed in place with four screws. The optional SD extension board for local data logging (Supplementary Fig. 3e, f) plugs into the main PCB through a board-to-board connector before the Airscope is mounted. Data acquisition begins upon attachment of the battery to the base plate. **b,** Versatility of Airscope. Airscope can be paired with a battery for fully wireless interrogation (left). It is also compatible with the traditional tethered mode, enabling longitudinal investigation (right).



Supplementary Fig. 6 | Evaluation of movement agility in mice wearing Airscope.

a, Representative movement trajectories of three mice in a 40×40 cm² open field. Each animal underwent two experimental conditions: Control group (without wearing Airscope) and Airscope group (wearing an Airscope along with a power supply battery). The black lines represent the trajectories over a 15-minute period, while the red square marks the 20×20 cm² central area. **b,** Accumulated movement distance over 15 minutes for eight animals in each group. The error bars represent standard deviations at twenty selected time points, marked by vertical lines. n =8 trials. **c,** Cumulative speed distribution over 15 minutes. Colors represent different groups, and different lines indicate individual trials. n = 8 trials. **d,** Box plots of median speed between the control and Airscope groups. The box elements include the median (central line), interquartile range (box), and whiskers indicating variability outside the upper and lower quartiles. Unpaired t-tests showed no

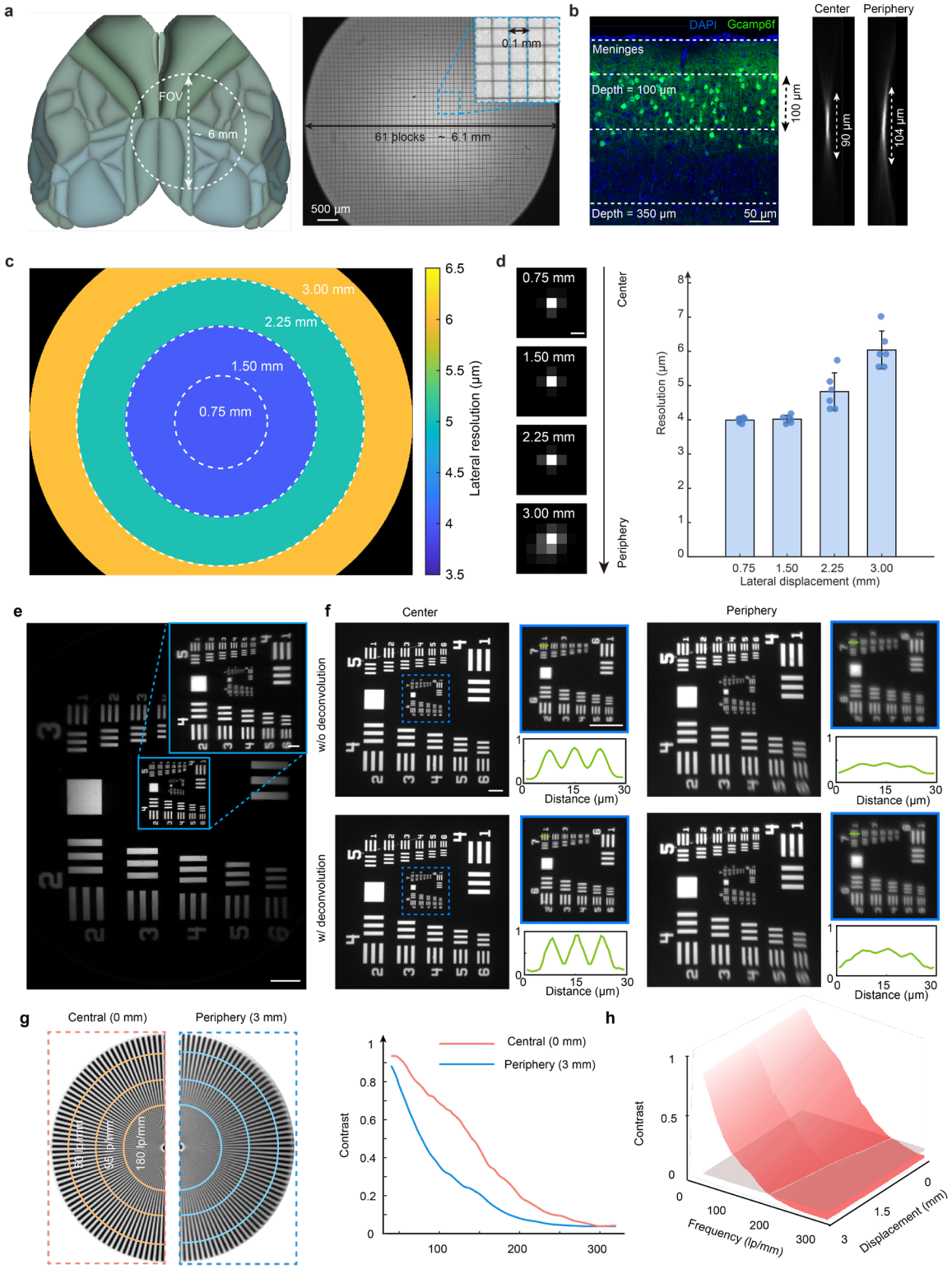
significant differences between the control and Airscope groups ($p = 0.485$, $n = 8$ trials). Supplement to Fig. 1n.



Supplementary Fig. 7 | High-resolution 3D skeleton reconstruction of a freely behaving animal wearing Airscope.

a, Schematic of the 3D capture setup. An eight-camera array surrounds the Airscope-equipped mouse to capture 360° visual data. **b,** Multi-view images of the animal captured simultaneously from eight cameras, with background removed using SAM2Mice. **c,** Kinematic modeling and 3D pose estimation. Left: The kinematic model with defined keypoints and skeletal structure. Right: A temporal sequence of 3D pose estimation. From top to bottom: The reconstructed 3D pose, the pose overlaid on the corresponding video frames, and a detailed view of the ear and eye keypoints. **d,** Neuronal imaging from Airscope. Top left: Standard deviation projection of Airscope movie.

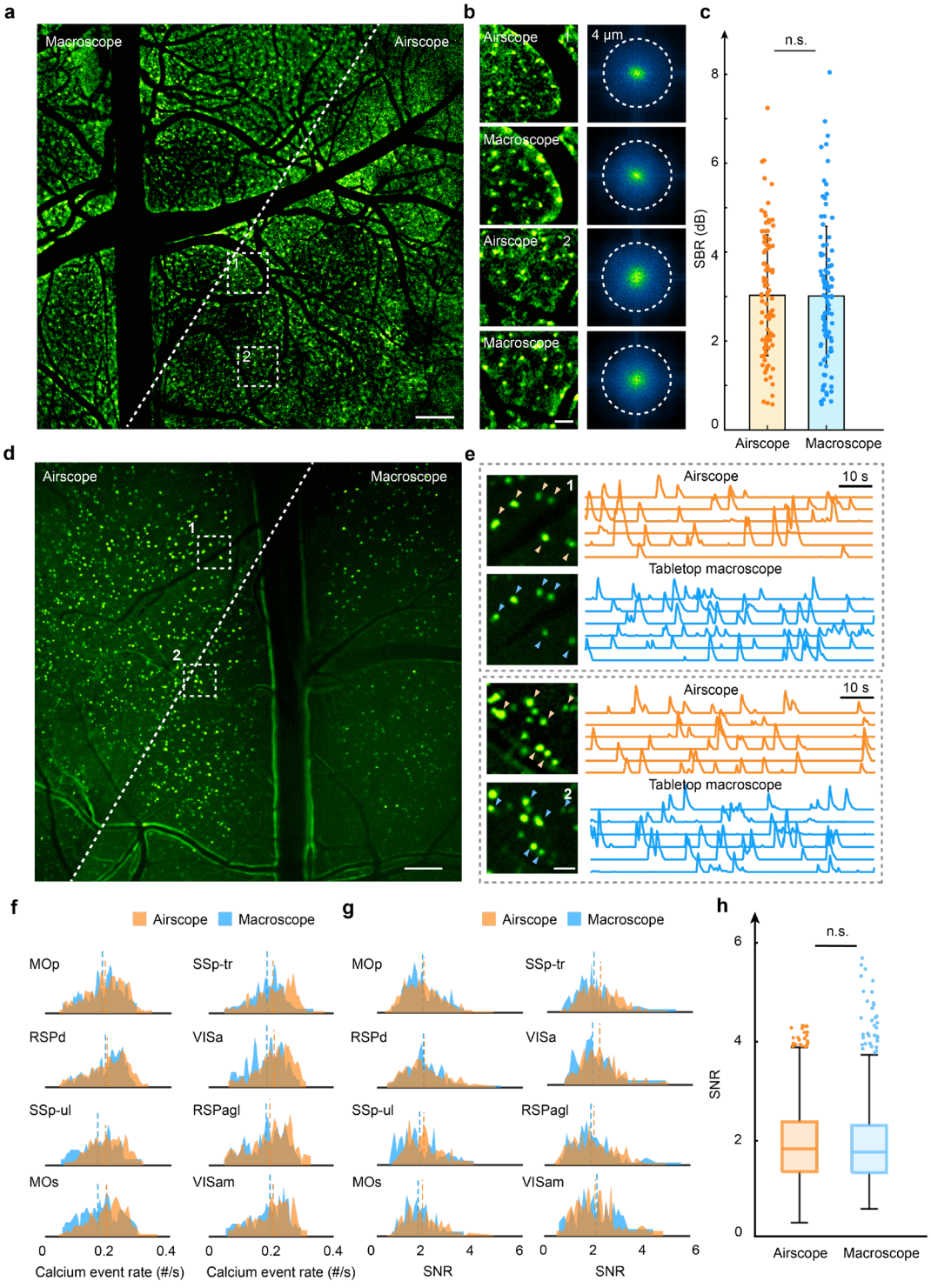
Right: Segmented neurons after the processing pipeline (Extended Data Fig. 4). **e,** Segmented neurons overlaid with Allen Common Coordinate Framework (CCF) atlas [18] with different colors representing different cortical regions. **f,** Heatmap of neuronal activities during animal freely behaving across different cortical regions. Two zoom-in panels illustrate representative neuronal traces from 50 neurons. **g,** 3D trajectories of each key point detected during animal freely behaving.



Supplementary Fig. 8 | Field of view and resolution characterization of Airscope.

a, Field of view (FOV) characterization. Left: schematic illustration of the 6 mm circular FOV over the mouse dorsal cortex. Right: field of view measurement using commercial fluorescent grid

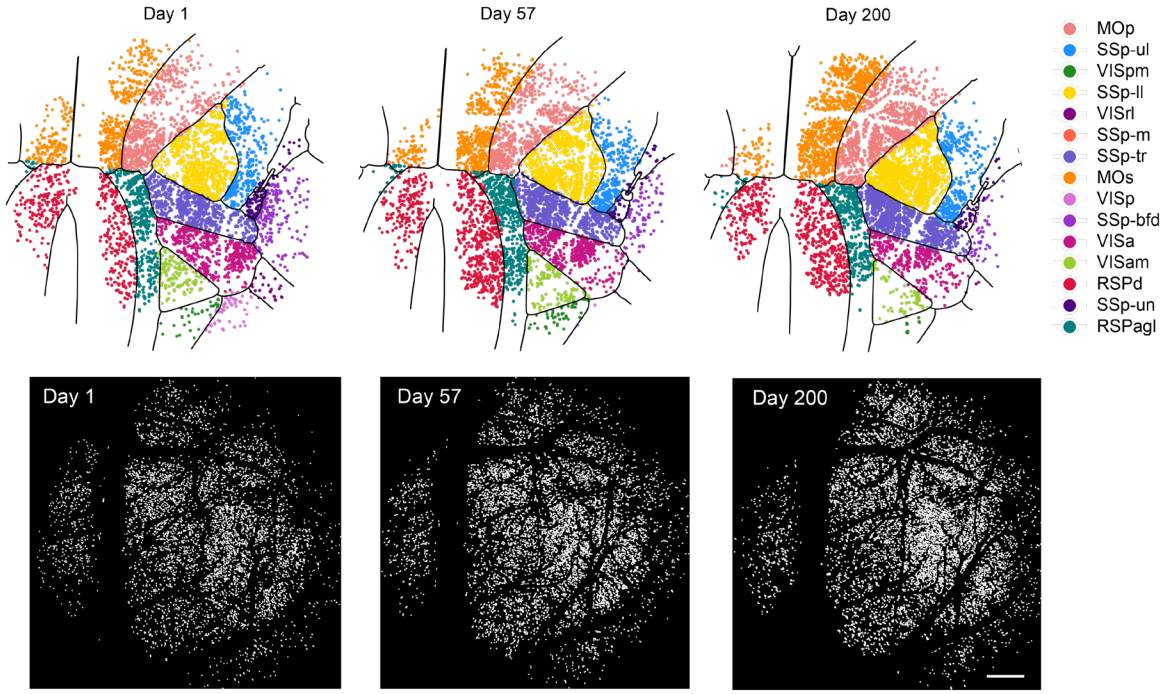
targets with a grid spacing of 0.1 mm. **b,** Depth of field characterization. Left: DAPI-stained brain section showing GCaMP6f expression in cortical neurons. Right: axial point spread function (PSF) profiles measured at the center and periphery of the FOV, showing effective depths of field. **c,** Lateral resolution characterized across the FOV; each region is color-coded according to the mean resolution value. **d,** Quantification of lateral resolution as a function of lateral displacement from the FOV center. Resolution was measured from imaged point emitters and averaged over two orthogonal directions (n = 6 per region, mean ± SD). Left: representative examples of the imaged point emitters. **e,** Full FOV imaging of a USAF resolution target, with a zoomed-in view shown on the top right panel. **f,** Imaging results (top) and corresponding Richardson–Lucy (RL) deconvolution results (bottom) of the USAF1951 resolution target acquired at the center (left) and periphery (right) from the center of the FOV. Zoom-in views of the blue dashed boxes are shown alongside each corresponding region, with intensity profiles extracted across the group 7, element 1 (7-1). **g,** Left panel: Siemens star MTF target acquired at the center and periphery (approximately 3 mm from the center) of the FOV. Right panel: Modulation transfer function (MTF) measured from Siemens star patterns at center (orange) and periphery (blue) of FOV. **h,** Surface plot of MTF variation across the FOV, representing the spatial distribution of focal plane resolution. The shaded section plane denotes the 0.1 contrast threshold. Scale bar: 500 μm (**a, e**), 100 μm (**f,** zoom-in area of **e** and **f**), 50 μm (**b**), 5 μm (**d**).



Supplementary Fig. 9 | Experimental performance of Airscope compared to a tabletop macroscope.

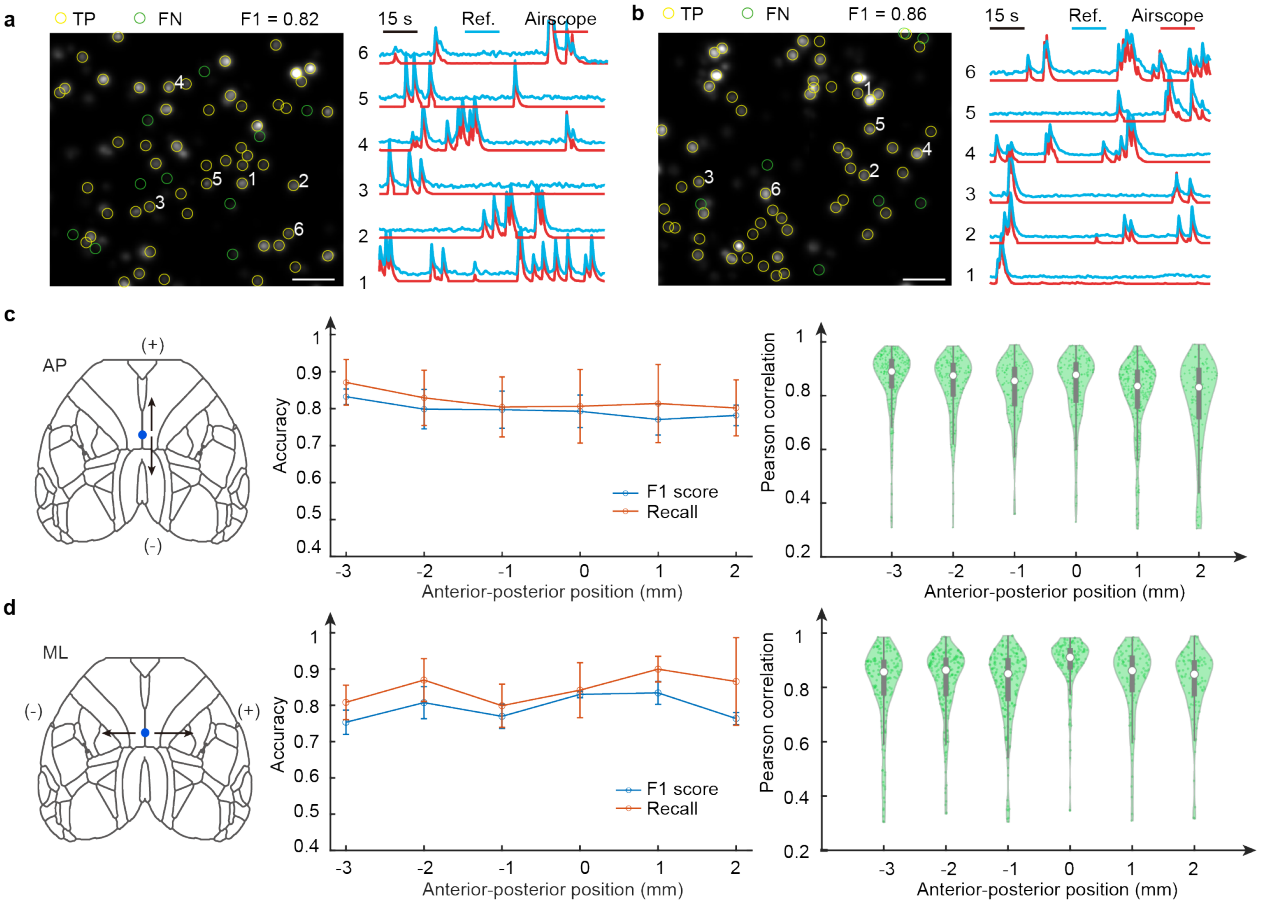
a, Comparison of microglia imaging in mouse brain between Airscope and a tabletop macroscope. **b,** Zoom-in views of the white dashed boxes are shown on the right, with corresponding Fourier

transform overlaid with Fourier rings at 4 μm in the frequency domain. **c,** Signal-to-background ratios (SBR) from the same microglia population imaged with Airscope and a tabletop macroscope. n = 100 cells. Height of bar, mean. Error bar, SD. Data points are overlaid. p = 0.74, n.s., not significant, two-sided Wilcoxon rank-sum test. **d,** Comparison of standard deviation projection of cortical imaging in Rasgrf2-dCre/Ai148D transgenic mice between Airscope and a tabletop macroscope. **e,** Left panel: Zoom-in views from Airscope and macroscope recordings at two different locations, marked by the white dashed boxes in panel **d**. Right panel: Neuronal activity traces, each corresponding to an arrow-labeled neuron in the zoom-in view. **f,** Histogram of calcium event rate recorded with Airscope (orange) and macroscope (blue) across multiple brain regions during a 2-minute recording session. **g,** Histogram of signal-to-noise ratio (SNR) recorded with Airscope (orange) and macroscope (blue) across multiple brain regions during a 2-minute recording session. **h,** Comparison of SNR of neuronal populations imaged by Airscope (orange) and macroscope (blue). No significant difference was observed (p = 0.782, two-sided Wilcoxon rank-sum test, 2470 data points acquired by Airscope, 1640 data points acquired by macroscope). Central line inside the box: median. Box: interquartile range. Whiskers: maximum and minimum. Points: outliers. Scale bar: 400 μm (**a** and **d**), 100 μm (**b**) and 20 μm (**e**); 10 seconds (**e**).



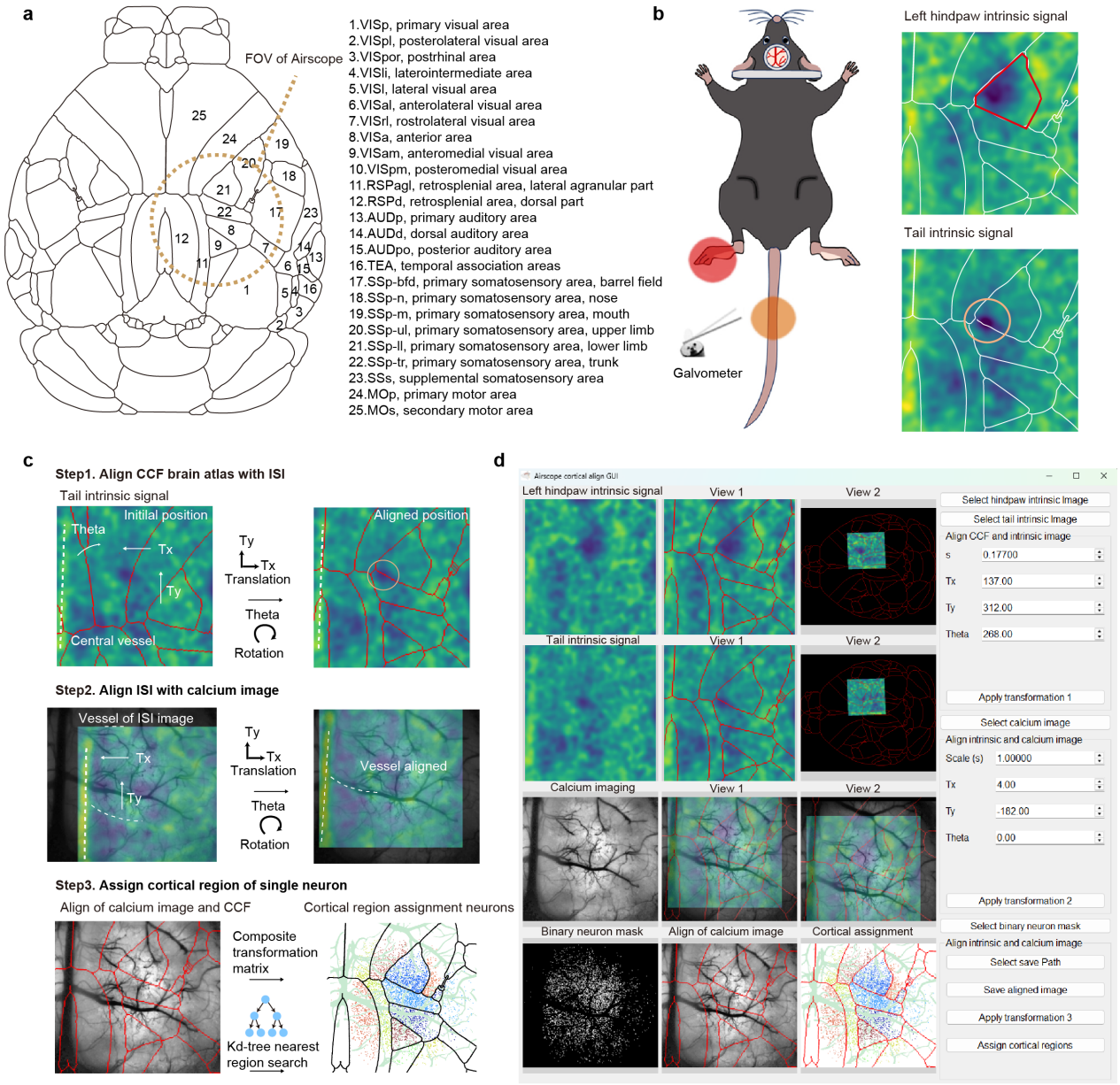
Supplementary Fig. 10 | Stable, long-term recordings enabled by Airscope.

Airscope enables stable, long-term recordings from the same neuronal population at a single site for over 200 days, circumventing macroscope limitations such as session-to-session animal repositioning and focus-plane drift. Scale bar: 400 μm.



Supplementary Fig. 11 | Hybrid 2p-Airscope recording over different lateral positions in dorsal cortex.

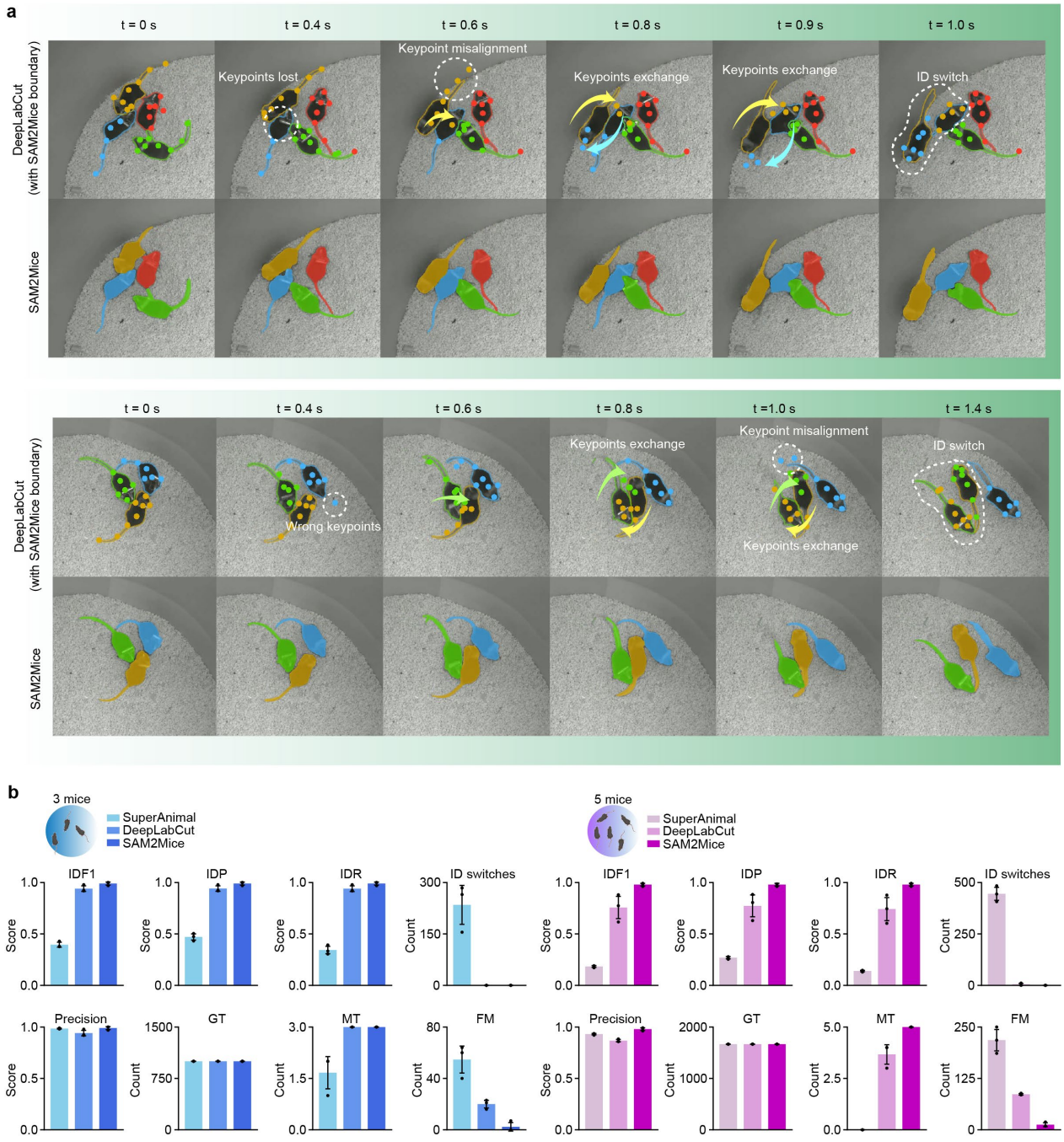
a-b, First column: Background-removed image overlaid with circular segments indicating true positives (TP, yellow) and false negatives (FN, green). Second column: Randomly selected calcium traces by two-photon microscope regarded as ground truth reference (blue) and Airscope (red). **c,** Evaluation of neuron-detection accuracy (F1 scores and recall) achieved by Airscope at different anterior-posterior (AP) positions (left panel). Circle: mean. Error bar: ±1 SD. Pearson correlation scores achieved by Airscope at different anterior-posterior (AP) positions (right panel). White circle: median. Thick gray vertical line: interquartile range. Thin vertical lines: upper and lower proximal values. Transparent disks: data points. Transparent violin-shaped areas: kernel density estimate of data distribution. **d,** Same evaluation of neuron-detection at different mediolateral (ML) positions as **c**. Scale bar: 50 μm (**a** and **b**).



Supplementary Fig. 12 | Intrinsic signal imaging-based brain region localization pipeline for Airscope.

a, Alignment of Airscope field of view (FOV) with Allen Common Coordinate Framework (CCF) whole-brain atlas [18]. The Airscope FOV is indicated in light yellow. **b,** Sensory stimulation protocol and corresponding intrinsic signal responses. Tail and hind paw were stimulated using a cotton swab (left) [19]. Heatmaps of intrinsic signals in response to hind paw (upper right) and tail (lower right) stimulation illustrate localized cortical activation. **c,** Neuron registration to the CCF using Airscope. Step 1: Intrinsic imaging maps are aligned to the CCF via affine transformation (rotation and scaling). Step 2: Intrinsic and calcium imaging data are affinely co-registered. Step 3: A

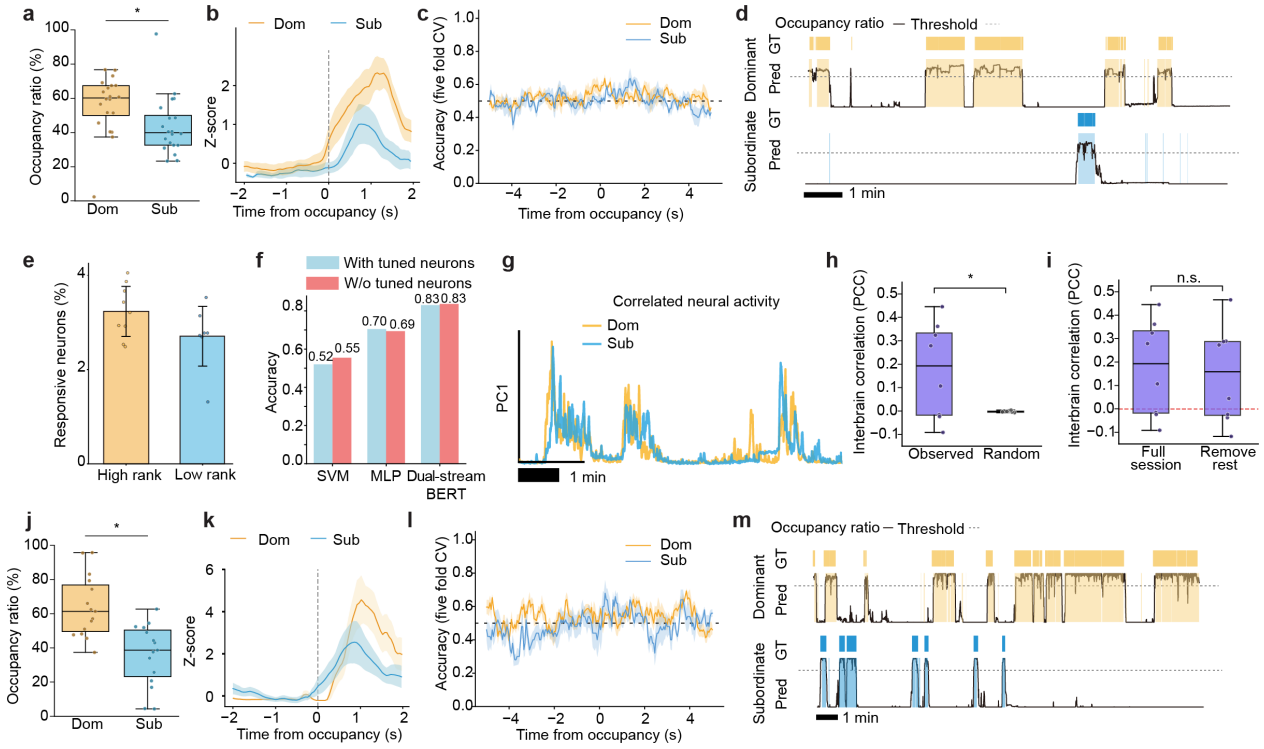
composite transformation matrix is computed to project neurons identified in calcium imaging into CCF coordinates, enabling precise brain region annotation. **d,** Custom graphical user interface (GUI) for registration workflow. The GUI provides a code-free approach for calculating transformation matrices, visualizing alignment of intrinsic and calcium images with the CCF, and mapping segmented neurons to specific brain regions.



Supplementary Fig. 13 | Comparison of multi-animal tracking between SAM2Mice and keypoint-based methods.

a, Side-by-side comparison of DeepLabCut[20] and SAM2Mice in tracking multiple animals in the open field test. Two cases with different animal numbers are presented. Problems such as keypoint lost (the tracker fails to detect a body part), keypoint misalignment (keypoints are placed on incorrect body locations), keypoint exchange (keypoints are swapped between animals during close interactions), and ID switch (the entire identities of animals are swapped) are highlighted. For

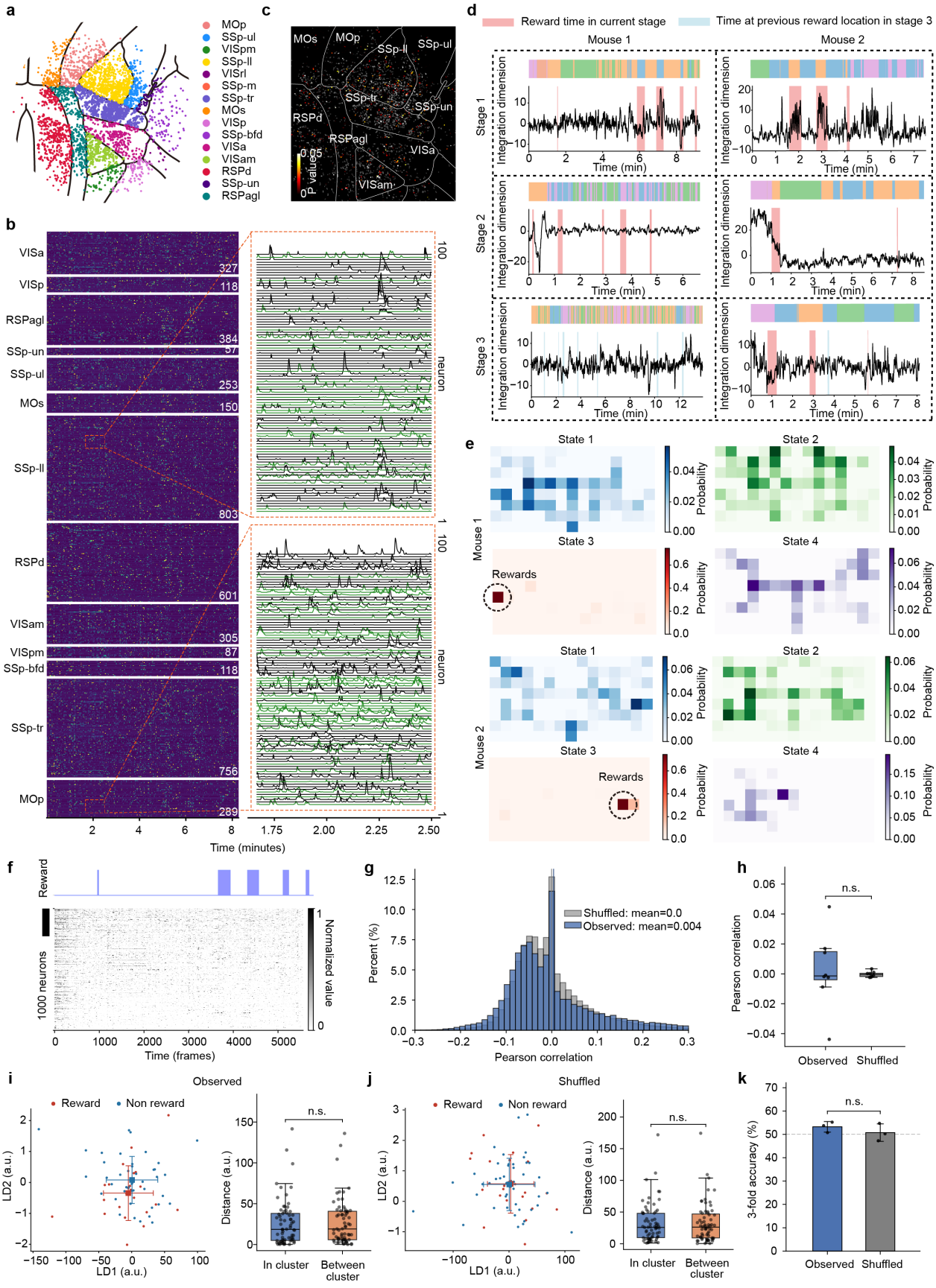
visualization, we overlay each animal with SAM2Mice-extracted segmentation contours. **b,** Quantitative benchmark SAM2Mice with SuperAnimal[21] and DeepLabCut. SuperAnimal was evaluated in a zero-shot setting using the official *superanimal_topviewmouse_x* checkpoint from the repository, whereas DeepLabCut was fully trained on the corresponding modality-specific datasets following the official training protocols. Left: Comparison of SuperAnimal (zero-shot), DeepLabCut (fully trained) and SAM2Mice (zero-shot) on a three-mouse tracking task in a 60 cm-diameter circular open field. Right: Same comparison as left, but performed on five mice. Performance was evaluated using three 333-frame video segments for both the three- and five-mouse cohorts. Bars, mean; error bars, SD; dots, video segments. Top row reported animal identity tracking metrics. IDF1 (Identification F1 Score): Harmonic mean of ID precision and recall, reflecting overall ID tracking accuracy. IDP (Identification Precision): Proportion of correctly identified detections among all predicted identities. IDR (Identification Recall): Proportion of correctly identified detections among all ground truth identities. ID switches: Number of times the tracker incorrectly assigns a new identity to a previously tracked object. Bottom row reported tracking accuracy and fragmentation metrics. Precision: Proportion of correct detections among all tracker outputs. GT: Total number of ground truth trajectories. MT (Mostly Tracked): Number of ground truth trajectories tracked for $\geqslant$80% of their duration (higher is better). FM (Fragmentation): Number of times a ground truth trajectory is interrupted due to tracking failure and reinitialization (lower is better). Supplement to Fig. 2r.



Supplementary Fig. 14 | Dorsal cortical activity patterns that distinguish dominant- and subordinate-animal trials during food and object-play competition.

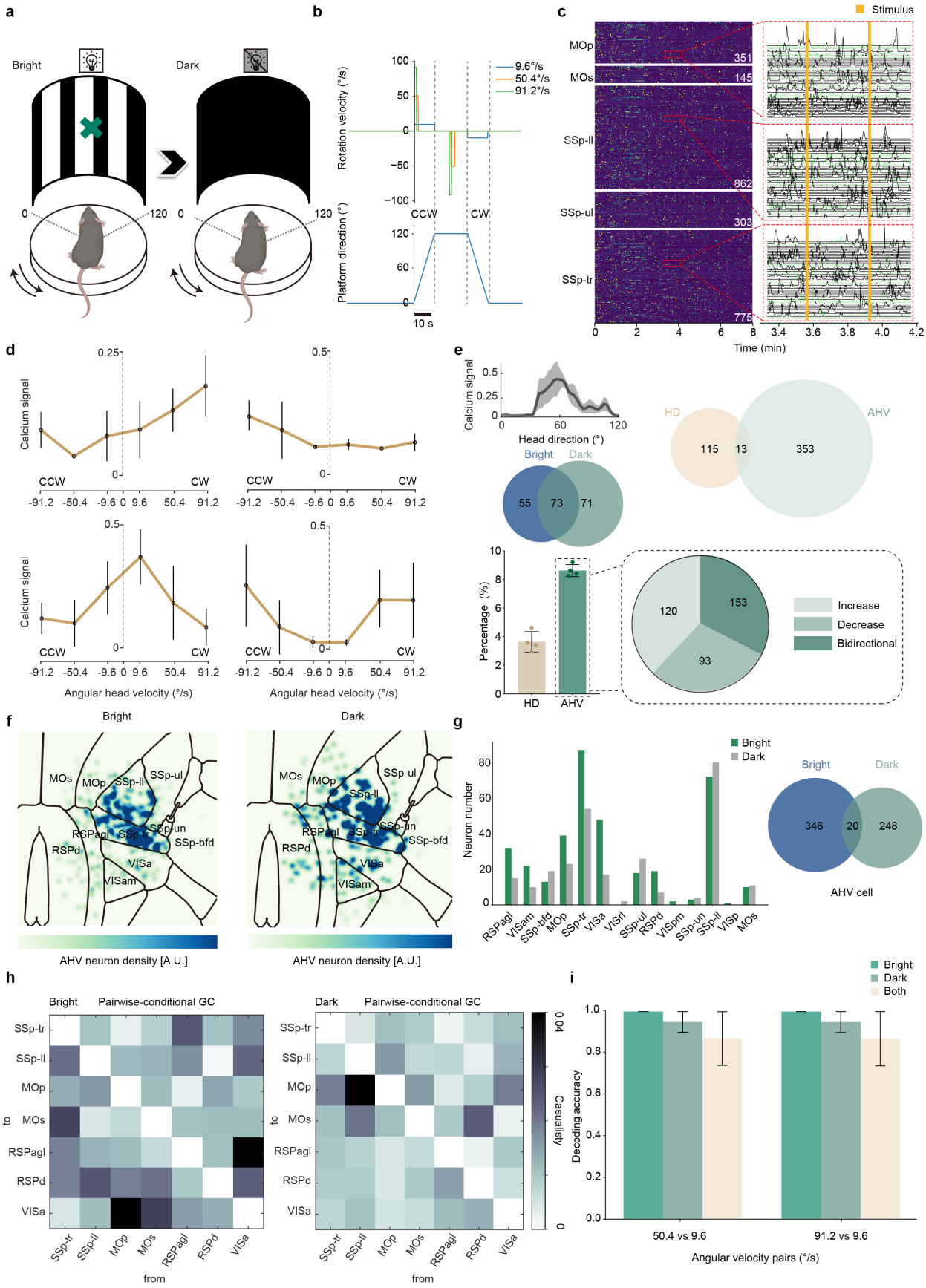
a, Box plot of food port occupancy for dominant and subordinate animals (n = 20 trials, 10 mice in total, ~15 minutes per trial; *p = 0.036, two-sided Wilcoxon test; center line, median; box, interquartile range; whiskers, 5th–95th percentiles; dots, trials). **b,** Z-scored peri-event neural activity for dominant and subordinate mice as they gain control of the port. Solid lines: Mean. Shaded area: ± SEM. **c,** Time-resolved LDA decoding accuracy for dominant and subordinate animals around port-occupancy onset, evaluated using five-fold cross-validation. Solid lines denote mean; shaded areas denote SEM. **d,** Temporal dynamics of foodport occupancy and predictor performance. Black traces denote observed occupancy ratios. Upper shaded regions mark periods when the observed ratio exceeded 0.8, while lower shaded regions indicate predicted occupancy intervals. Results are shown for both dominant and subordinate. **e,** Percentage of feeding-responsive neurons in high-rank and low-rank animals (n = 9 high-rank mice and 7 low-rank mice). Bars show mean ± SD; dots indicate individual animals. **f,** Decoding accuracy and F1 scores for SVM, MLP and dual-stream BERT classifiers with or without feeding-tuned neurons. **g,** Example PC1 activity traces from two animals engaged in feeder competition, obtained by applying principal component analysis to dorsal cortex-wide neuronal population activity. **h**, Interbrain correlations

in interacting pairs or correlations of randomly permuted traces during feeder competition (n = 8 recording sessions, two-sided Wilcoxon rank-sum test, *p = 0.023). Box plots show median and interquartile range; whiskers indicate the data range; dots, sessions. **i**, Interbrain correlations during the full feeder competition session and after removing concurrent rest epochs (n = 8 recording sessions). Box plots show median and interquartile range; whiskers indicate the data range; dots, sessions. Two-sided Wilcoxon rank-sum test, p = 0.645. **j–m,** Analogous analyses to **a–d** for competition over a toy running wheel, with occupancy of the object as the behavioral metric (**j**: n = 15 trials; 10 mice in total; dots indicate individual trials). Scale bar: 1 minute (**g**) and (**m**).


a
MOp
SSp-ul
VISpm
SSp-ll
VISrl
SSp-m
SSp-tr
MOs
VISp
SSp-bfd
VISa
VISam
RSPd
SSp-un
RSPagl
c
MOs
MOp
SSp-ll
SSp-ul
SSp-tr
SSp-un
RSPd
RSPagl
VISa
VISam
0.05
0
P values
b
VISa
VISp
RSPagl
SSp-un
SSp-ul
MOs
SSp-ll
RSPd
VISam
VISpm
SSp-bfd
SSp-tr
MOp
327
118
384
97
253
150
803
601
305
87
118
756
289
neuron
Time (minutes)
d
Reward time in current stage
Time at previous reward location in stage 3
Mouse 1
Mouse 2
Stage 1
Stage 2
Stage 3
Integration dimension
Time (min)
e
State 1
State 2
State 3
State 4
Mouse 1
Mouse 2
Rewards
Probability
f
Reward
1000 neurons
Normalized value
Time (frames)
g
Shuffled: mean=0.0
Observed: mean=0.004
Percent (%)
Pearson correlation
h
n.s.
Pearson correlation
Observed
Shuffled
i
Observed
Reward
Non reward
LD2 (a.u.)
LD1 (a.u.)
n.s.
Distance (a.u.)
In cluster
Between cluster
j
Shuffled
Reward
Non reward
LD2 (a.u.)
LD1 (a.u.)
n.s.
Distance (a.u.)
In cluster
Between cluster
k
n.s.
3-fold accuracy (%)
Observed
Shuffled

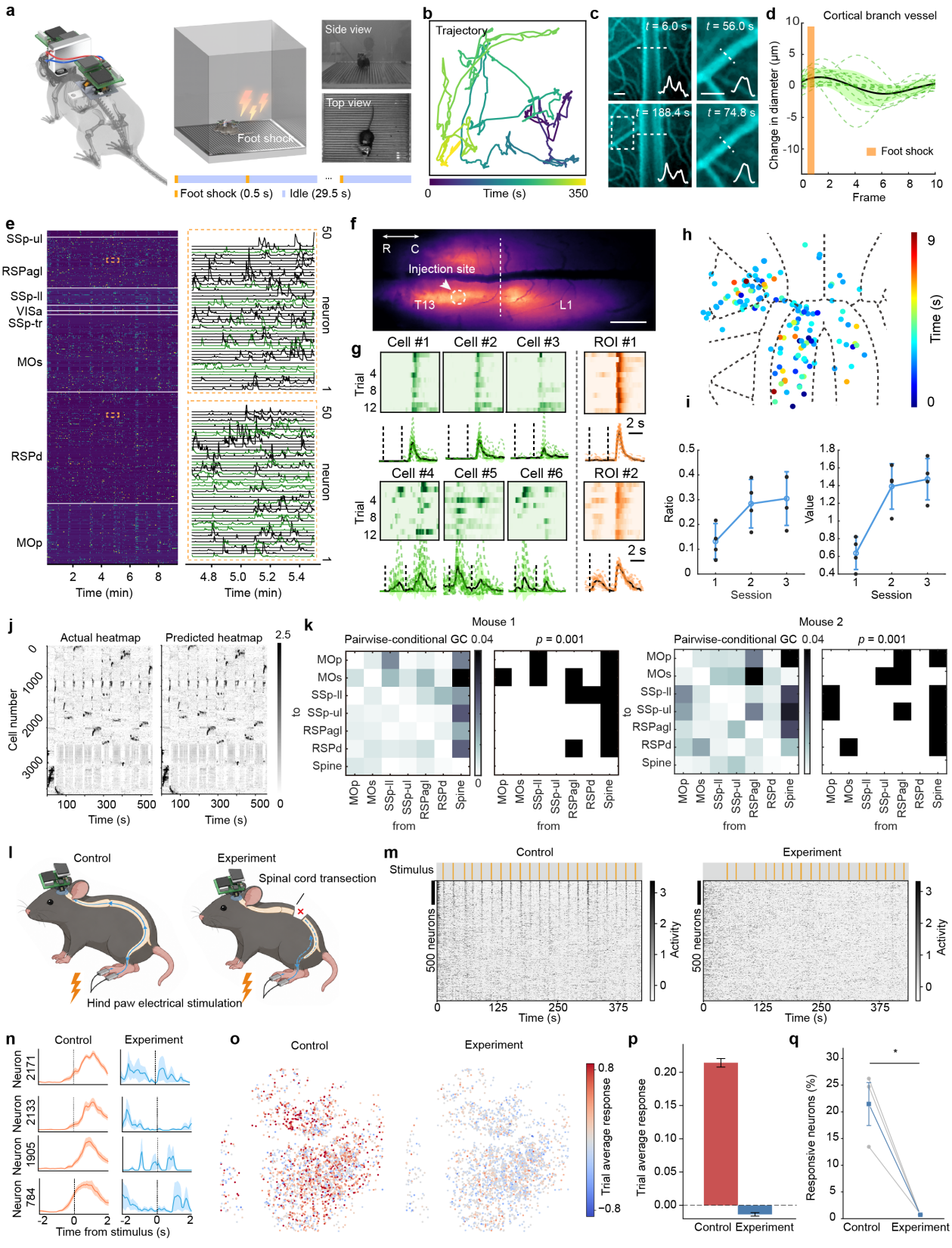
Supplementary Fig. 15 | Cortical population activity recorded by Airscope during labyrinth exploration.

a, Segmented neurons overlaid with Allen CCF atlas [18] with different colors representing different cortical regions. **b,** Temporal activity heat map of inferred neurons. Two zoom-in panels show example traces (each with 100 neurons). Neurons are randomly sorted in each cortical region. **c,** Distribution of the neurons that respond to turning left or right during exploration in the maze across the dorsal cortex. **d,** Temporal composition of inferred latent states (top) and integration dynamics overlaid with reward receipt (bottom, reward as red shaded region) in a representative trial. In stage 3, animal visitation of prior reward location is marked as blue shaded region. Supplement to Fig. 5h for two other mice. **e,** Spatial visualization of rSLDS-inferred latent states. For each state, spatial probability is plotted during the animal moving across the maze. The top four states are exhibited. Supplement to Fig. 5j for two other mice. **f,** Example calcium activity heatmap during maze exploration, with reward-associated frames marked in blue. **g,** Histogram of Pearson correlations between individual-neuron activity and reward state for observed and shuffled data. Both distributions are centred near zero. **h,** Boxplot of average Pearson correlation for recorded sessions between observed and shuffled controls (two-sided Wilcoxon rank-sum test, $p = 0.878$, $n = 8$ sessions from 3 animals). Centre line, median; box, interquartile range (IQR); whiskers, most extreme values within 1.5 × IQR of the box. Dots represent individual sessions. n.s., not significant. **i**, Left, LDA projection of population activity in observed data for validation set, with reward frames shown in red and non-reward frames shown in blue. Right, boxplot of within-cluster and between-cluster distances (two-sided Wilcoxon rank-sum test, $p = 0.725$, $n = 67$ per distribution, from 8 sessions across 3 animals). Centre line, median; box, interquartile range; whiskers, most extreme values within 1.5 × IQR of the box. Dots represent frames. **j,** Same analysis as **i** for shuffled data (two-sided Wilcoxon rank-sum test, $p = 0.940$, $n = 3$ animals, $n = 67$ per distribution, from 8 sessions across 3 animals). **k,** 3-fold cross validation accuracy of LDA for distinguishing reward from non-reward frames in observed and shuffled data (two-sided Wilcoxon rank-sum test, $p = 0.5$). n.s., not significant. Bar plots represent mean ± SD and dots denote folds.


a
Bright
Dark
0
120
b
Rotation velocity (°/s)
9.6°/s
50.4°/s
91.2°/s
CCW
CW
Platform direction (°)
10 s
c
Stimulus
MOp
MOs
SSp-ll
SSp-ul
SSp-tr
351
145
862
303
775
Time (min)
d
Calcium signal
CCW
CW
Angular head velocity (°/s)
e
Calcium signal
Head direction (°)
Bright
Dark
55
73
71
HD
AHV
115
13
353
Percentage (%)
120
153
93
Increase
Decrease
Bidirectional
f
Bright
Dark
MOs
MOp
SSp-ll
SSp-ul
SSp-un
SSp-tr
SSp-bfd
RSPagl
RSPd
VISa
VISam
AHV neuron density [A.U.]
g
Neuron number
Bright
Dark
RSPagl
VISam
SSp-bfd
MOp
SSp-tr
VISa
VISrl
SSp-ul
RSPd
VISpm
SSp-un
SSp-ll
VISp
MOs
346
20
248
AHV cell
h
Bright
Dark
Pairwise-conditional GC
SSp-tr
SSp-ll
MOp
MOs
RSPagl
RSPd
VISa
to
from
Causality
i
Bright
Dark
Both
Decoding accuracy
50.4 vs 9.6
91.2 vs 9.6
Angular velocity pairs (°/s)

Supplementary Fig. 16 | Cortical responses to vestibular rotational stimulation recorded by Airscope under light and dark conditions.

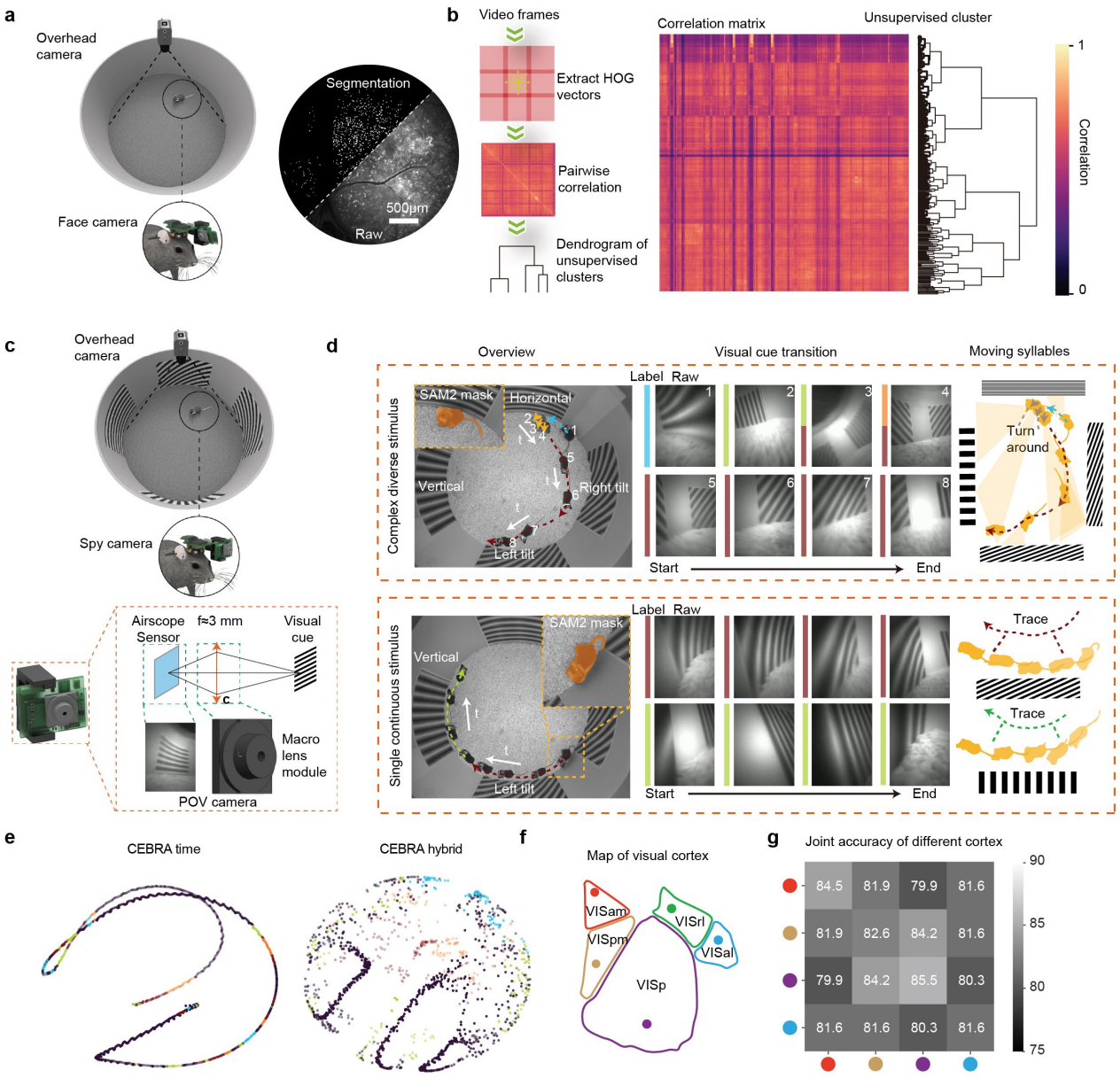
a, Schematics of vestibular test. Mice were first recorded under light conditions while the rotary platform rotated back and forth four times from 0 to 120° at constant velocity. Visual landmark was located at 60°. Then the rotation was repeated in dark conditions without visual cues. **b,** Three angular velocities (9.6°/s, 50.4°/s, and 91.2°/s) in either clockwise (CW) or counterclockwise (CCW) directions used in the trials. **c,** Heatmap of neuron activity across different cortical regions during rotational stimulation. Two zoom-in panels show example traces (each with 50 neurons). Neurons are randomly sorted in each cortical region. **d,** Four distinct single-neuron tuning types observed during rotational stimulation. Mean ± SD. n =4 trials. Cells exhibiting tuning specificity to a particular angular head velocity (AHV) are defined as AHV-tuned cells. **e,** Top left: Example of a head direction (HD) cell (top) and evidence demonstrating the consistency of HD cells (n = 73 cells) across bright (n = 128 cells) and dark (n = 144 cells) conditions in a single animal. Top right: Venn diagram showing overlap of HD cells (n = 128) and AHV cells (n = 366) across cortical recordings in one mouse (n =12 trials). Bottom left: Summary data showing the percentage of cells tuned to HD or AHV in one mouse. Bottom right: Pie chart showing proportions of AHV cells (n = 366) with bidirectional or unidirectional (increase and decrease) tuning. **f,** Spatial distribution of AHV cells across multiple brain regions. A salt-and-pepper pattern with SSp-II and SSp-tr predominance can be observed from bright (left) to dark (right) conditions. **g,** Left: Distribution of AHV cells across brain regions differs between bright and dark conditions. Right: AHV cells also show a small amount of overlap in both bright and dark conditions. **h,** Granger causality analysis between brain regions in bright (left) and dark (right) conditions, suggesting different causal connections under each condition. **i,** Rotation speed pairs decoding accuracies using LSTM (50.4°/s vs. 9.6°/s and 91.2°/s vs. 9.6°/s, three-fold per mouse, two mice; n = 6, mean ± SEM) using AHV cells divided into three groups (only bright responsive, only dark responsive, and responsive in both bright and dark). Scale bar: 10 seconds (**b**).


a
Side view
Top view
Foot shock
Foot shock (0.5 s)
Idle (29.5 s)
b
Trajectory
Time (s)
0
350
c
t = 6.0 s
t = 56.0 s
t = 188.4 s
t = 74.8 s
d
Cortical branch vessel
Change in diameter (μm)
Foot shock
Frame
e
SSp-ul
RSPagl
SSp-ll
VISa
SSp-tr
MOs
RSPd
MOp
neuron
Time (min)
f
R
C
Injection site
T13
L1
g
Cell #1
Cell #2
Cell #3
ROI #1
Cell #4
Cell #5
Cell #6
ROI #2
Trial
2 s
h
Time (s)
i
Ratio
Value
Session
j
Actual heatmap
Predicted heatmap
Cell number
Time (s)
k
Mouse 1
Mouse 2
Pairwise-conditional GC
p = 0.001
MOp
MOs
SSp-ll
SSp-ul
RSPagl
RSPd
Spine
to
from
l
Control
Experiment
Spinal cord transection
Hind paw electrical stimulation
m
Control
Experiment
Stimulus
500 neurons
Activity
Time (s)
n
Control
Experiment
Neuron 2171
Neuron 2133
Neuron 1905
Neuron 784
Time from stimulus (s)
o
Control
Experiment
Trial average response
p
Trial average response
Control
Experiment
q
Responsive neurons (%)
Control
Experiment

Supplementary Fig. 17 | Simultaneous cortex and spinal cord imaging for interrogation of vascular and neuronal dynamics.

a, Schematic of dual-Airscope mounted over brain and spinal cord for concurrent observation during foot shock stimulation. Right panel: Representative side- and top-view camera recordings of animal behavior. **b,** Locomotor trajectory within the chamber, color-coded by time. **c,** Zoomed-in panels of cortical vascular imaging at different time points. White curves show the intensity profiles along the white dashed lines, which indicate the vessel diameter. Right panel shows the zoom-in view of the white dashed box region on the left. **d,** Diameter changes of branch vessel in cortex after foot shock stimulus. Bold lines: Mean. Shaded area: SD. Orange bar: Stimulus onset. Supplement to Fig. 6d. **e,** Heat map of inferred neuronal activities during simultaneous brain and spinal cord population activity recording. Two zoom-in panels show example traces (each with 50 neurons). Neurons are randomly sorted in each cortical region. **f,** Imaging results of spinal cord population activity in freely moving mice, delineating T13 and L1 segments (dashed white lines) and indicating the viral injection site (dashed circles). R represents rostral direction and C represents caudal direction. **g,** Neural responses to stimulus in brain (green) and spinal cord (orange). Heatmaps show trial-aligned responses across 12 trials. Solid lines: mean response; shaded areas: SD. Dashed colored lines indicate individual trials; dashed black lines indicate cue and foot shock timing. Supplement to Fig. 6h with different neurons and ROIs. **h,** Dorsal cortex-wide neuron distribution color-coded by response latency to the foot shock stimulus. **i,** Left: ratio of cue-evoked response to foot shock-evoked response of spinal cord components. Right: absolute response amplitudes of spinal cord components following cues. Mean $\pm$ SD. ($n = 4$ spinal components per session, each averaged over 12 trials). Supplement to Fig. 6k. **j,** Raster map of observed neuronal activities (left) and predicted neuronal activities (right) through linear dynamic system modeling. Supplement to Fig. 6l. **k,** Left: Granger causality matrix depicting directed interactions among cortical regions during fear conditioning ($n = 59$ trials for 2 mice in total). Right: statistically significant causal links ($p < 0.001$, corrected Granger F test) are shown in black; nonsignificant interactions are unfilled. **l,** Spinal cord transection experimental design. **m,** Population neuron activity heatmaps aligned to repeated hindpaw stimulation epochs (orange lines) for control and spinal-transected mice. Neurons are matched across sessions by neuron registration and sorted according to their trial average responses. **n,** Example stimulus-aligned calcium responses from the same registered neurons shown before and after spinal transection. Center lines

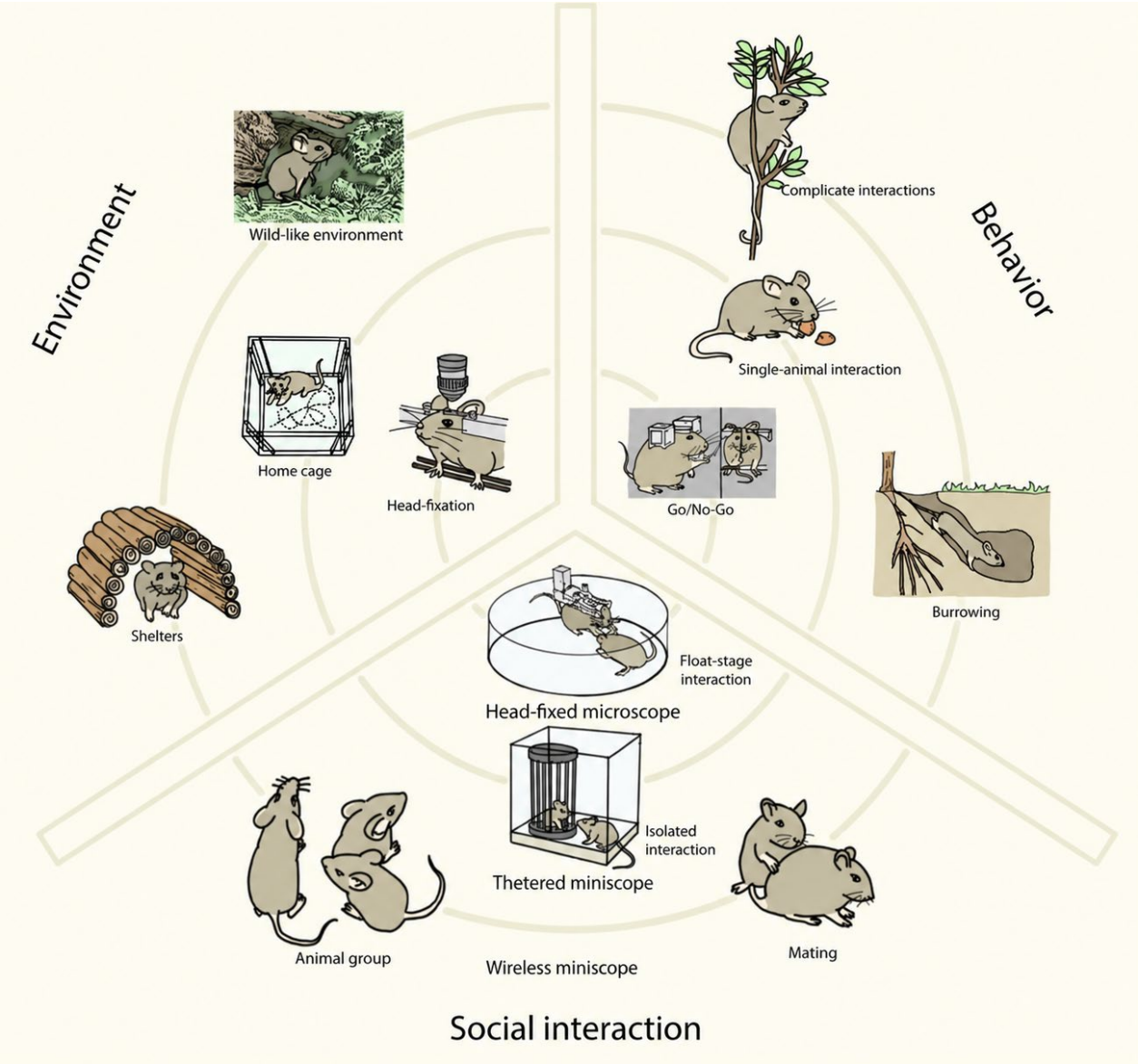
indicate mean and shaded areas indicate SEM across trials. Dashed lines indicate stimulus onset. **o,** Spatial distribution of trial-averaged stimulus responses in control and transected conditions. Each dot represents one neuron, color-coded by trial-averaged response amplitude. **p**, Bar plot of single-neuron trial-averaged responses in control and spinal-transected mice (4,772 registered neurons from n = 3 mice; mean ± SEM). **q,** Fraction of stimulus-responsive cortical neurons in each animal before and after spinal transection (paired t-test, *p = 0.0369). Grey lines indicate individual animals; blue error bars indicate mean ± SEM. Supplement to Fig. 6m. Scale bar: 100 μm (**c**), 500 μm (**f**), 2 s (**g**), 500 neurons (**m**).



Supplementary Fig. 18 | Simultaneous multimodal imaging using dual Airscopes in freely behaving mice.

a, Left: Schematic of experimental setup. A mouse equipped with dual Airscopes moves freely in a round arena with diameter of 60 cm, while the brain activities and facial dynamics are continuously monitored through Airscope and its modified version with a macro lens to capture the orofacial expression (Methods). Right: segmented neurons (left) and standard deviation projection of Airscope movie (right). **b,** Clustering analysis of facial expression. Left: Workflow for frame-wise clustering of facial expressions from video recordings. Right: Pairwise similarity matrix (left) and hierarchical clustering dendrogram (right) identifying distinct expression clusters

through unsupervised learning. **c,** Experimental setup of an open-field arena with visual cues in the wall. Mice were fitted with both the Airscope and a modified version incorporating a macro lens to capture the environment from the animal's visual perspective. The 60 cm-diameter circular arena featured four distinct wall patterns serving as visual landmarks, while overhead camera recordings tracked locomotor trajectories. **d,** Visual stimulus presentation and behavioral paradigms. Two distinct modes were observed: In the first (top row), animals actively scanned the environment during locomotion; in the second (bottom row), animals maintained a relatively stable head position while briefly fixating on visual stimuli. **e,** CEBRA-based embeddings of neural activity. Neural activity embeddings based on temporal features (left), and hybrid representations integrating both behavior and temporal features (right). Supplement to Extended Data Fig. 10k. **f,** Structural organization of the visual cortex. **g,** Joint classification accuracy across visual cortex subregions using kNN reveals dominant contribution of VISp in visual stimulus decoding. Scale bar: 500 μm (**a**).



Supplementary Fig. 19 | Neuronal imaging in fully unrestrained animals using the Airscope system.

Conventional head‐fixed imaging confines animals to restricted movements and permits only rudimentary social interactions−one animal remains stationary under the microscope while a conspecific may approach. Tethered miniscope systems free animals from head fixation and allow exploration of simple home-cage environments and more complex behaviors; however, simultaneous recordings from two tethered animals remain challenging. By contrast, our wireless Airscope fully liberates the animal: it can navigate virtually any environment, perform intricate tasks, and engage in unrestricted group interactions—all while delivering high-quality cortical

imaging. Animal can now explore almost any conditions, performing any complicated tasks. Social interactions are also unrestricted, enabling complex social behaviors and group interactions.

Supplementary Tables

Supplementary Table 1 | A comparison of open-source and commercial devices, highlighting key optical, digital and mechanical specifications. We sort miniaturized microscopes based on their fields of view (FOVs). Throughput (pixels s^{-1}): total pixels transmitted per second (frame × width × height / frame interval). Spatial bandwidth: FOV (mm^2) divided by square of half of lateral resolution (μm^2), reflecting the total resolvable area (Methods). NA: not available or not applicable. The computation of space bandwidth product of the miniaturized microscope has taken into account the differential lateral resolutions throughout the entire field of view[22].

Year	Name of techniques	Imaging	FOV (mm)	Resolution (μm)	Frame Rate (Hz)	Weight (g)	Height (mm)	Width (mm)	Volume (cm^3)	Throughput (pixels/s)	Spatial bandwidth product	Spatiotemporal bandwidth product
2017	**FHIRM-TPM**[23]	2P	0.13×0.13	0.64	40	2.15	20	16.25	3.25	2.6×10^6	1.65×10^5	6.60×10^6
2024	**TINIscope**[24]	1P	0.45×0.45	3	40	0.43	8.24	13.8	0.52	5.18×10^6	9×10^4	3.60×10^6
2018	**CHEndoscope**[25]	1P	0.5×0.5	2	20	4.5	20	NA	NA	5.54×10^7	2.5×10^5	5.00×10^6
2022	**MINI2P**[26]	2P	0.5×0.5	1.15	15	2.4	25	15.2	5.78	9.83×10^5	7.56×10^5	1.13×10^7
2025	**M-MINI2P**[27]	2P	0.5 × 0.5	1.34	81.5	<3	25	15.2	5.78	5.34×10^6	5.57×10^5	4.54×10^7
2019	**Wireless Miniscope**[28]	1P	0.5×0.5	2.5	10	3.9	30	18	8.64	4.00×10^5	1.6×10^5	1.6×10^6
2026	**2P/3P multiplane miniscope**[29]	2P/3P	0.45 × 0.60	1.30(3P)	9.73	2.5	NA	NA	NA	6.78×10^6	2.69×10^6	2.62×10^7
2018	**UCLA Miniscope v3**[4]	1P	0.70×0.45	3	30	3.0	22.5	13	1.98	1.08×10^7	1.4×10^5	4.20×10^6
2020	**Miniscope Wirefree**[30]	1P	0.7×0.45	3	20	3.9	24	17.05	2	2.05×10^6	1.4×10^5	2.80×10^6
2020	**NINscope**[31]	1P	0.79×0.50	3	30	1.6	18.2	11	2.2	1.44×10^7	1.67×10^5	5.01×10^6
2011	**Integrated Miniscope**[32]	1P	0.8×0.6	2.5	36	1.9	20	11	2.4	1.11×10^7	3.07×10^5	1.11×10^7
2016	**UCLA Miniscope**[33]	1P	0.8×0.6	3	30	3.0	22	12	1.98	1.08×10^7	2.13×10^5	6.39×10^6

2017	**FinchScope**[34]	1P	0.8×0.6	3	30	1.8	16	8.5	1.16	9.22×10^{6}	2.13×10^{5}	6.39×10^{6}
2018	**Doric µScope**	1P	0.73×0.73	2	45	3.7	16.6	13.9	2.52	1.79×10^{7}	5.33×10^{5}	2.40×10^{7}
2014	**Inscopix nVista**[35]	1P	0.75×0.9	2.08	20	2.2	22	15	2.28	1.92×10^{7}	6.24×10^{5}	1.25×10^{7}
2021	**UCLA Miniscope v4**[5]	1P	Φ 1.0	3	30	2.6	22.3	16.9	5.88	1.08×10^{7}	3.49×10^{5}	1.05×10^{7}
2023	**Featherscope**[36]	1P	1.0×1.0	4-7	30	1.0	15	16.5	1.24	1.44×10^{7}	2.5×10^{5}	7.50×10^{6}
2025	**MINIXL**[37]	1P	Φ 3.5	4.4	23	3.5	30	15	7.5	2.3×10^{7}	1.99×10^{6}	4.58×10^{7}
2023	**MiniLFOV**[38]	1P	3.6×2.7	3.5–6.2	11	13.9	38	40	12	5.54×10^{7}	1.97×10^{6}	2.17×10^{7}
2023	**Kiloscope**[36]	1P	4.8 × 3.6	6	30	1.4	15	17	2.04	1.44×10^{7}	1.92×10^{6}	5.76×10^{7}
2025	**Airscope**	1P	Φ 6	4-6	12.5	1.0	8.15	13	1.45	2.40×10^{7}	4.68×10^{6}	5.85×10^{7}

Supplementary Table 2 | Comparative analysis of wireless recording devices, focusing on the number of neurons each can record.

NA: not available or not applicable. Shaded green rows exhibit devices used for mice.

Logger model / system	Approx. weight (g)	Channels	Estimated cell yield (single units or neurons)	Evidence & notes
Wireless telemetry system [39]	≈6 (≈12 g with battery)	4	~5–20 units	Yartsev & Ulanovsky built a ~12 g head-mounted logger that transmitted action potentials from a tetrode (4 channels) while the bats flew freely.
MouseLog-16 MouseLog-16B (Deuteron Technologies)	1.9 g logger board (≈3.5 g with battery)	16	~50–80 units	Deuteron's MouseLog-16 is a 16-channel logger weighing 1.9 g (board only). With a 40-mAh battery the total mass is roughly 3.5 g.
RatLog-128 (Deuteron Technologies)	≈3.4 g (1.92 g board + 1.5 g headstage; battery extra)	128	~300–500 units	Modular logger for rats. Board weighs 1.92 g; each headstage (16–128 channels) weighs ~1.5 g.
SpikeLog-128 (Deuteron Technologies)	4.4 g including memory card	128	~300–500 units	Single-board logger with 128-channel 16-bit ADC; weight 4.4 g.
SpikeGadgets Neuropixels Datalogger headstage	19.2 g headstage (≈31 g with 400-mAh battery)	400	~400–700 units	Headstage logs up to 400 channels from a Neuropixels probe; weight ~19.2 g without battery.
WES 2.0 (Wireless Electrophysiology System)[40]	0.95 g (without battery) / ~3.19 g with 100-mAh Li-ion battery	12-32	~20–80 units	Open-source wireless system with flexible sampling rates. The wearable module weighs 0.95 g and ~3.19 g with a 100-mAh battery.
FreeLynx (Neuralynx)	11.5 g device; typical 21.3 g with battery and 64-ch AFE	Up to 256	~300–500 units	Neuralynx's battery-powered logger supports up to 256 channels; device mass ~11.5 g.
CerePlex W (Blackrock Neurotech)	26.4 g (33.5 g with battery)	96	~150–300 units	Wireless headstage for Blackrock arrays; 96-channel wideband recording; weight 26.4 g without battery and 33.5 g with battery.
JAGA Penny (Jinga-hi)	1.1 g (device only)	4	~4–12 units	Penny-size wireless neural logger; 4-channel unit-recording at 10 kS/s or EEG at 1 kS/s.

RCB-W24B-LVDS (DSP Wireless)	19 g (without battery) and ~31.7 g with battery	32	~60–120 units	WiFi-enabled headstage for 32 RHD channels; brochure lists headstage weight 19 g and 31.7 g with battery.
Doric FiWi wireless headstage	≈2g (2.8 g including battery)	4	~10–20 units	Fiberless & wireless system for rodents; 4-channel recording at 14.3 kHz; mass 2.8 g with 60-mAh battery.
Multichannel Systems W-series headstages	W4-HS ~1.9 g, W8-HS 2.9 g, W16-HS 3.6 g, W32-HS 3.7 g (all without battery)	4, 8, 16 or 32	~10–120 units	Wireless headstages from Multi Channel Systems; the W32-HS provides 32 channels and weighs ~3.7 g without battery.
ELG-2 EEG/EMG logger (Teleopto/Amuza)	16-h version ≈1.9 g; 26-h version ≈2.4 g	Up to 7 channels	NA (EEG/EMG telemetry)	Head-mounted EEG/EMG logger storing data on a microSD card. Teleopto notes a 1.9 g logger for 16 h recording and a 2.4 g version for 26 h; a high-speed variant offers 5 signal channels plus reference and ground.
Miniscope Wirefree[30]	3.9 g without battery	NA	~300 neurons	A standard Miniscope V3 can typically record from hundreds of neurons simultaneously, with reported figures often ranging from approximately 100 to 300 neurons.
Wireless miniScope	3.9 g without battery	NA	~200 neurons	A wireless miniScope for deep brain imaging in freely moving mice.[28]
Finchscope	1.8 g without battery	NA	~300 neurons	An open source, wireless capable miniature microscope system.[34]
wScope	2.7 g without battery	NA	~300 neurons	Cable-free brain imaging for multiple free-moving animals with miniature wireless microscopes.[41]
Airscope	1 g without battery	NA	>= 8,500 neurons	See Fig. 2 of manuscript

Supplementary Table 3 | Parts list of Airscope.

	Part	Description / CAD file name	Vendor	Quantity	Unit Price (USD)
Main PCB	ESP32-PICO-V3-02	Microcontroller Unit	Espressif	1	4
	OV2640	CMOS sensor	OmniVision	1	2.5
	AN2051-245	Antenna	Rainsun	1	0.2
	MAX31875	Temperature sensor	Analog Devices	1	1
	PTPS7A2028PDQNR	2.8V LDO for CMOS sensor	TI	1	0.3
	PTPS7A2015PDQNR	1.5V LDO for CMOS sensor	TI	1	0.3
	LM36011	LED driver	TI	1	0.3
	BM29B0.6-2DS	Connector to LED-FPC and power-FPC	Hirose Electric	2	0.2
	DF40C-20DP	Connector to extension PCB	Hirose Electric	1	0.3
	PCB	Main.kicad_pcb	JLC	1	7
Extension PCB	CSNP32GCR01-AOW	On board SD chip	CS Semiconductor	1	5
	LSM6DSLTR	Inertial measurement unit	STMicroelectronics	1	1.2
	QMC6310	Magnetometer	QST	1	0.6
	DF40HC-3.5-20DS	Connector to main PCB	Hirose Electric	1	0.3
	PCB	Extension.kicad_pcb	JLC	1	4
LED FPC	LXZ1-PB01	Blue excitation LED	Lumileds	4	4
	BM29B-0.6-2DP	Connector to main PCB	Hirose Electric	1	0.2
	PCB	LED.kicad_pcb	JLC	1	4
Power FPC	TPS63031	3.3V buck-boost converter	TI	1	0.8
	YZR0153-18023-01	Pogo pins to battery	Xinyangz	1	0.2
	BM29B-0.6-2DP	Connector to main PCB	Hirose Electric	1	0.2
	Magnet	3 mm diameter, 1mm height	Xinchi	2	0.25
	PCB	Power.kicad_pcb	JLC	1	4
Battery	401119	100mAh battery	Jinxunwei	1	1.3
	Magnet	3mm diameter, 1mm height	Xinchi	2	0.2
Optical assembly	Lens assembly	Customized Lens assembly	Sunny Optics	1	2
	440-477 nm_Ex	Excitation filter	Rayan Optics	4	4
	505-560 nm_Em	Emission filter	Rayan Optics	1	4
	M2 screw	For focal fixation	Helifouner	4	0.1
	Main body	Main_body.stl	Formlabs	1	NA
	Baseplate	Baseplate.stl	CNC	1	NA

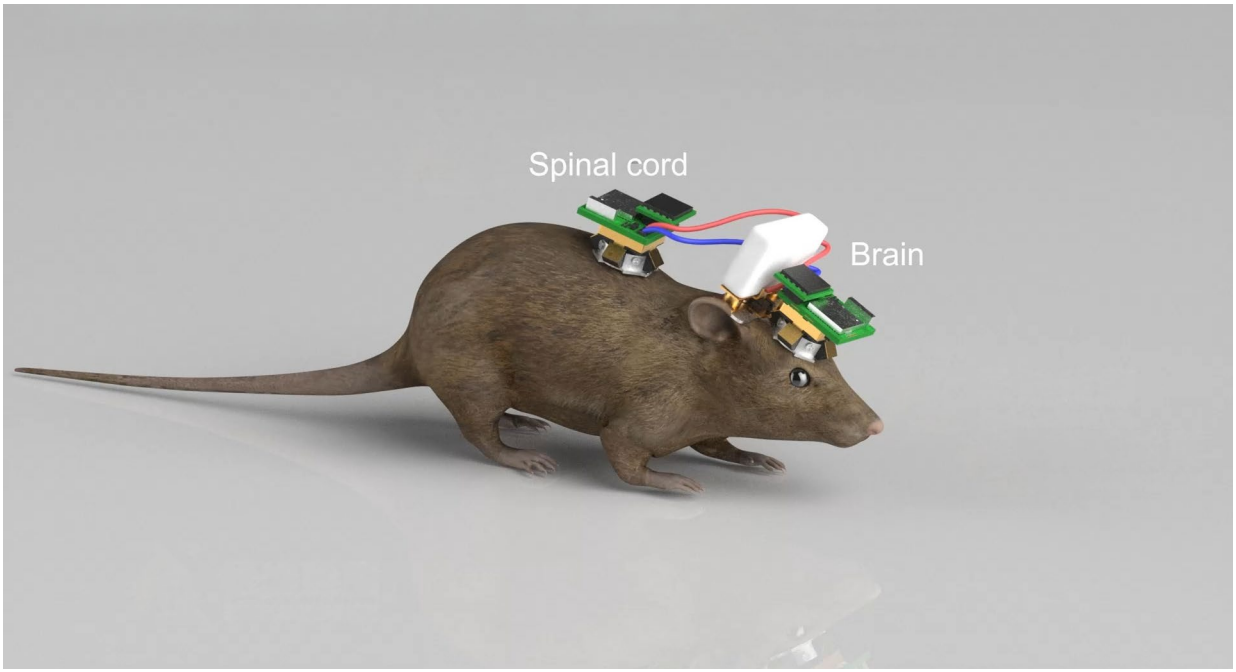
Total: 77.4 USD

Supplementary Table 4 | Component weight of Airscope.

Component	Measured parts	Mass (g)
Mechanical part	Housing	0.1670
Optical module (lenses + filters)	Lens + Em filter + Ex filter ×4	0.1121
Image sensor + PCB	PCB	0.5970
LED illumination module	LED	0.0941
Total (microscope only)		**0.9702**
Encapsulation	Glue	<0.05
Total (after encapsulation)		**1.0093**
SD card (optional)	SD card	0.3175
Battery (optional)	Battery (1.7 g config)	1.7323

Supplementary Videos

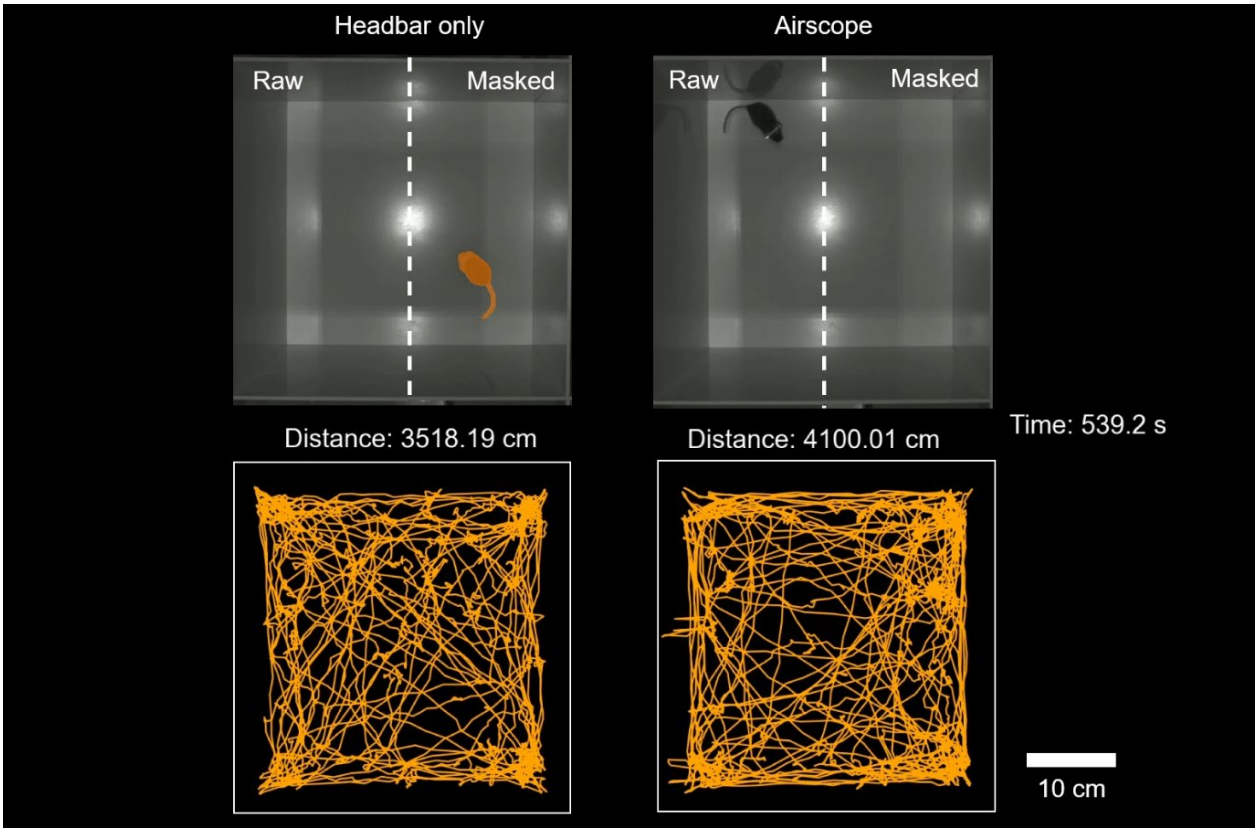
Supplementary Video 1



Overview of the Airscope.

Airscope assembly workflow and wireless neuronal recording. Part 1: A freely moving mouse equipped with Airscope is shown, followed by device assembly, LED illumination, fluorescence collection, rapid battery exchange, battery-powered operation, onboard SD-card storage, and real-time neuronal preview on a computer via Wi-Fi. Part 2: Representative neuronal imaging acquired with Airscope. Scale bar, 500 μm. Part 3: Representative applications, including simultaneous recordings from multiple freely interacting mice in a 5 m^2 open habitat and dual-site imaging within a single mouse using two Airscopes to record cortical and spinal cord activity simultaneously.

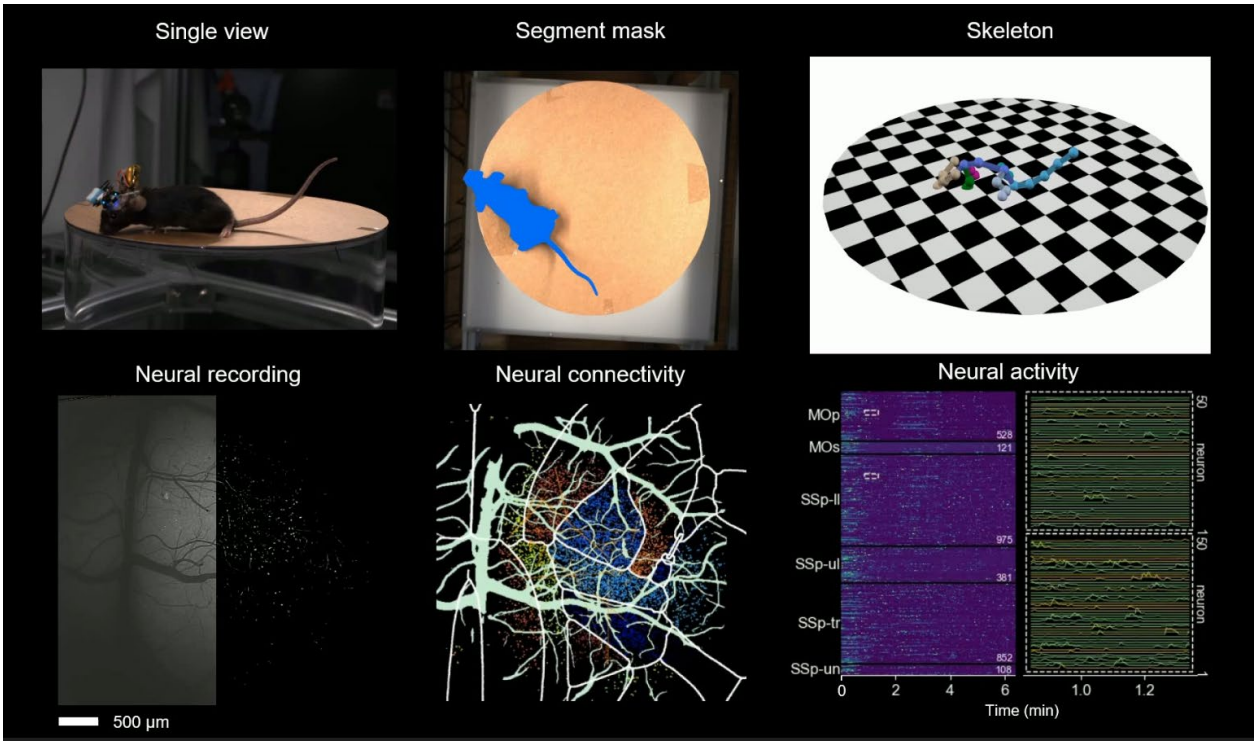
Supplementary Video 2



Assessing Airscope's impact on freely moving behavior.

Animals were evaluated in a 400 × 400 × 300 mm^3 open-field arena both with a head-bar only (left panels) and while wearing the Airscope (right panels). Top row: Representative raw video frames processed by SAM2Mice for automated animal segmentation. Bottom row: Corresponding motion trajectories extracted from the segmented videos. Scale bar: 10 cm.

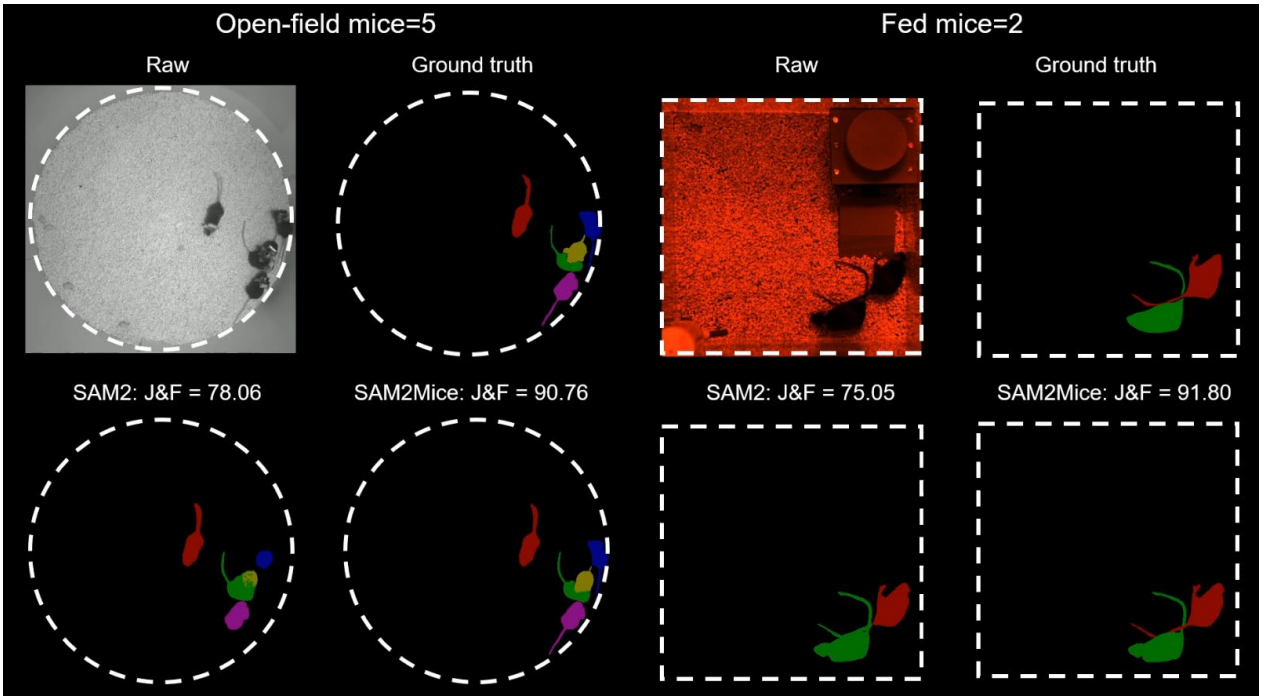
Supplementary Video 3



Airscope neural recording with high-resolution 3D reconstructed skeletons.

Top left: Side-view video of a mouse wearing Airscope, recorded by eight surrounding cameras. Top middle: Overhead behavior video with SAM2Mice segmentation. Top right: 3D skeletons reconstructed from multi-camera views[42]. Bottom left: Raw and background-removed calcium imaging. Bottom middle: Frame-wise single-neuron connectivity calculated using a 100-frame sliding window, with opacity indicating connection strength. Bottom right: Heatmap of neural activity across brain regions, with example neuronal traces from two regions. Scale bar, 500 μm.

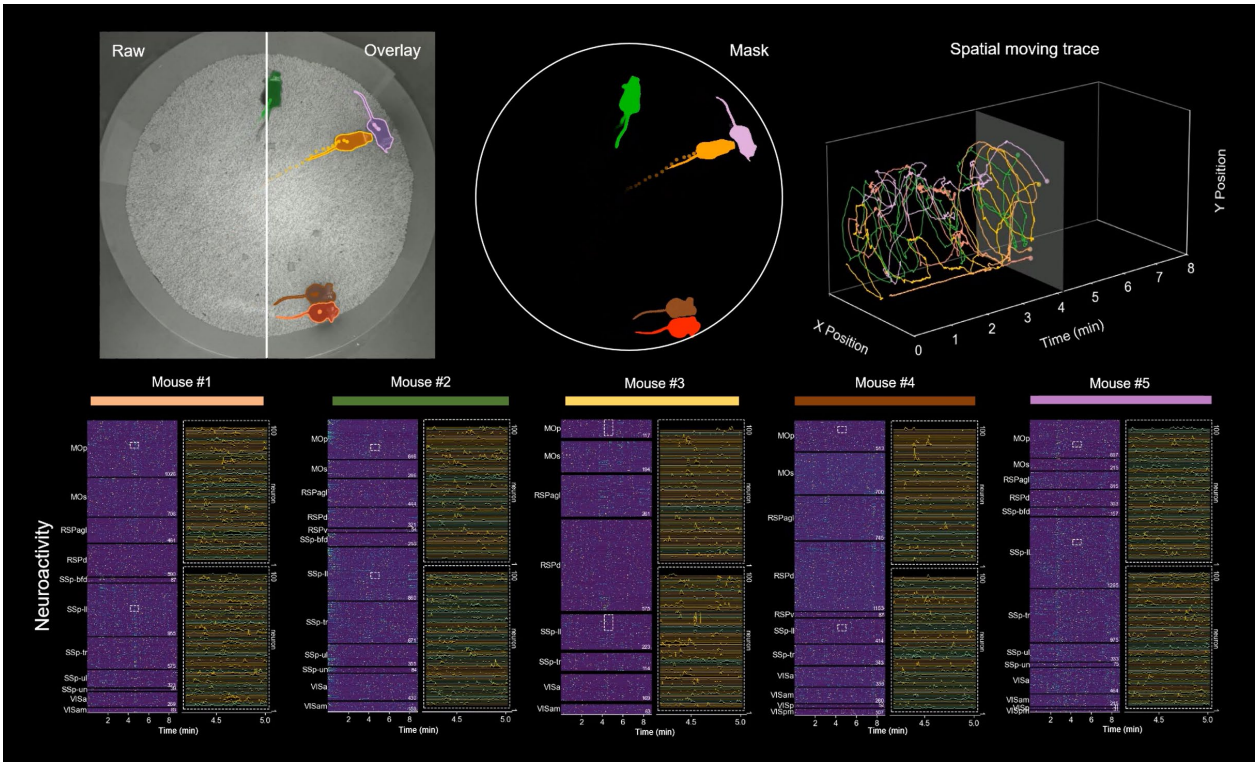
Supplementary Video 4



Robust zero-shot segmentation and identity tracking through SAM2Mice.

Part I: Zero-shot SAM2Mice segmentation of multiple mice in open-field and food-competition scenarios, compared with ground truth and SAM2. Part II: Prompt-free segmentation using YOLO v11-generated identity prompts in a 2.3 × 2.3 m habitat. Part III: Robust zero-shot performance across diverse behavioral environments. Part IV: Dynamic identity tracking during sequential animal appearance, compared with DeepLabCut. Part V: Multi-animal segmentation for three and five mice, compared with SuperAnimal and DeepLabCut. SAM2Mice maintains robust segmentation and consistent identities under crowded conditions. J&F denotes mean Jaccard index and F-score.

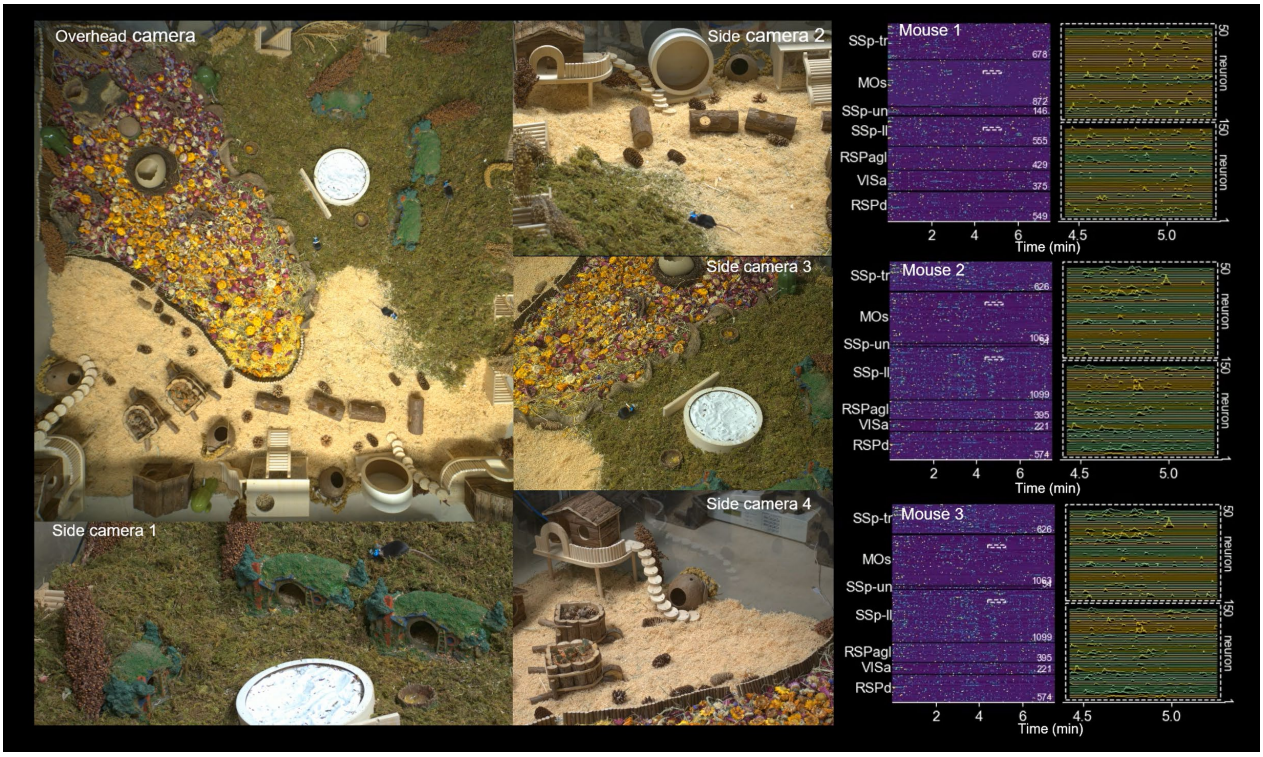
Supplementary Video 5



Simultaneous animal group recording with Airscope and multi-animal instance segmentation using SAM2Mice.

Top left: Five freely moving mice wearing Airscopes in a 60-cm circular arena, shown as raw video and SAM2Mice segmentation. Dots indicate 2-s centroid trajectories, and highlighted boundaries mark close social interactions (<2 cm). Top middle: Identity-coded segmentation masks with 2-s trajectories. Top right: 3D X–Y–time trajectories derived from mask centroids. Bottom: Simultaneous Airscope recordings from five mice, comprising 21,397 neurons. Heatmaps show cortical neural dynamics with representative calcium traces. Bar colors correspond to animal identities defined by the segmentation masks.

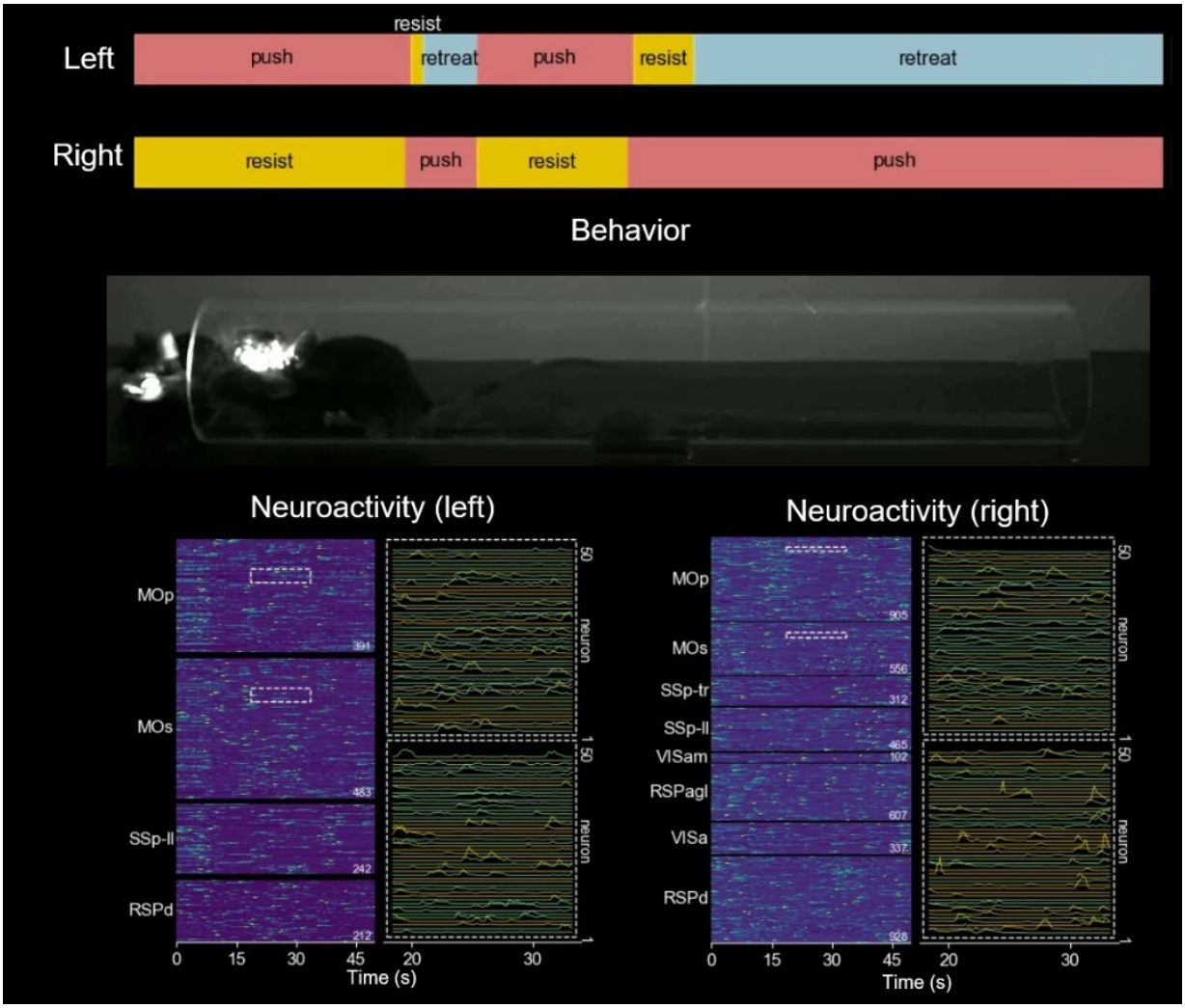
Supplementary Video 6



Animal groups wearing Airscope freely exploring large-scale, complex naturalistic environments.

Left: Multi-angle videos of a 2.3 × 2.3 m naturalistic habitat containing sandy, floral, and grassland zones, enriched with tree hollows, shelters, staircases, and running wheels. The camera array enables comprehensive behavioral tracking of Airscope-equipped mice from multiple perspectives. Right: Simultaneous Airscope recordings from three freely moving mice. Each panel shows cortex-wide neural activity heatmaps, with enlarged insets displaying representative neuronal calcium traces over time.

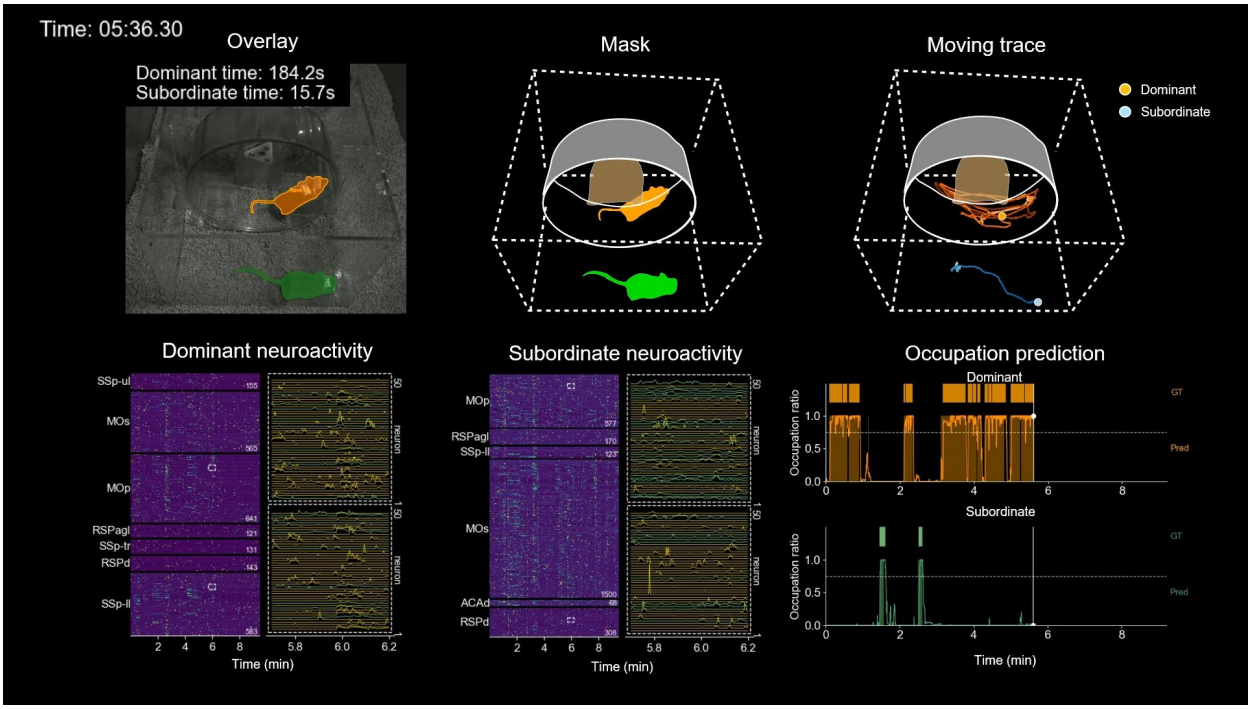
Supplementary Video 7



Neural recording of social hierarchy competition in tube test through Airscope.

Top: Frame-wise manual annotation of tube test social behaviors, capturing the full sequence from the initial still phase to the outcome of the winner, with labeling of four behavioral categories: push, resist, retreat, and still. Middle: Side view of the competitive tube assay. Mice were implanted with Airscope, enabling simultaneous neural recording during social competition. The compact Airscope design permitted unrestricted animal movement within the tube. Bottom: Synchronized calcium signal recordings from both mice. Left panel shows multi-region activity heatmap, with right panels highlighting detailed neuronal traces over time.

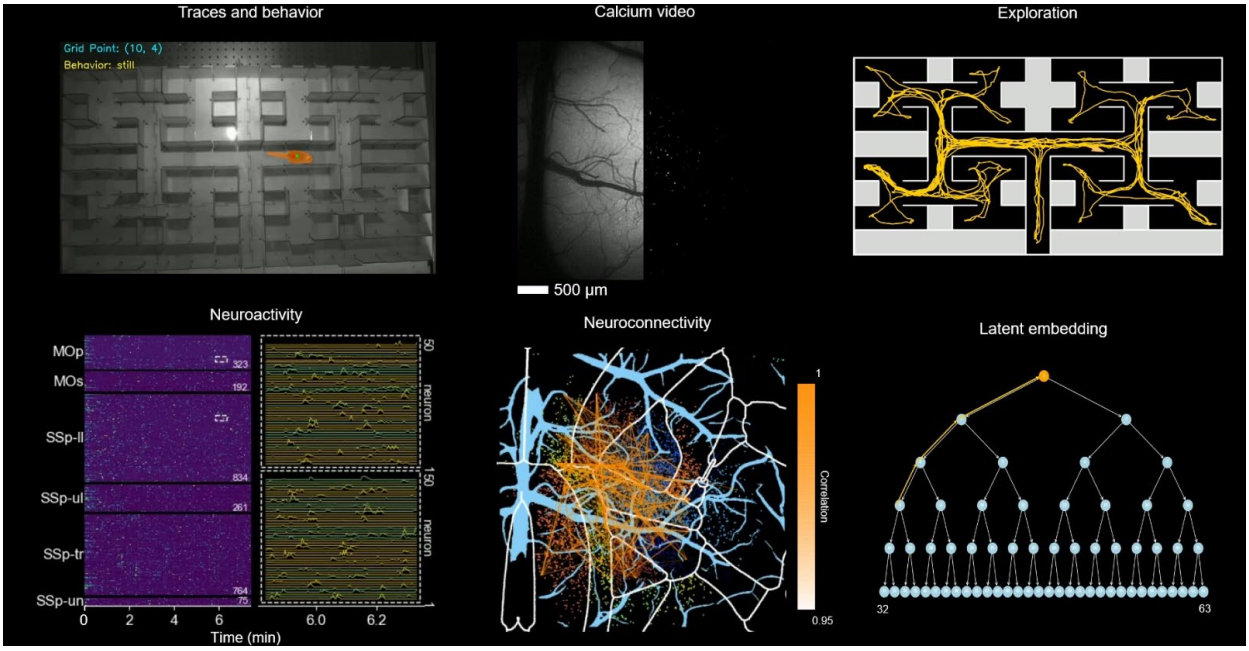
Supplementary Video 8



Neural recording of object-play and food competition through Airscope.

Part I: Object-play competition. Top: Side-view video with SAM2Mice masks of dominant (orange) and subordinate (green) mice, segmented masks, and 10-s movement trajectories; mask boundaries are highlighted during wheel occupancy. Bottom: Multi-region neural activity from both mice, with inset calcium traces, and wheel occupancy quantified by SAM2Mice (GT) and model prediction. Dominant and subordinate occupancy ratios are shown in orange and green, respectively; dashed lines indicate 0.8. Part II: Food competition. Same layout and analysis as in Part I, applied to food competition.

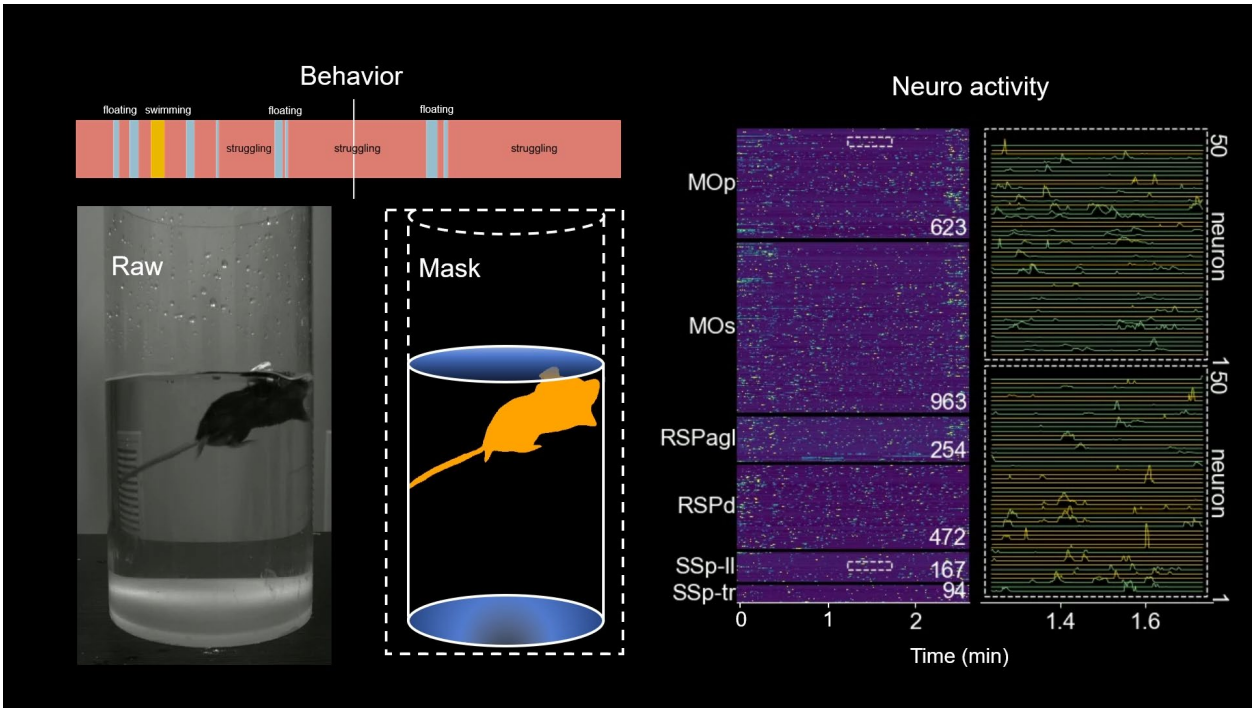
Supplementary Video 9



Neural recording of an animal freely exploring a complex maze with Airscope.

Top left: Airscope-equipped mouse navigating a 15 × 8 binary maze with SAM2Mice segmentation, showing current position and behavioral state. Top middle: Raw and background-removed calcium imaging. Top right: Movement trajectory with velocity-scaled arrows. Bottom left: Cortical neural activity heatmaps with representative neuronal traces. Bottom middle: Frame-wise single-neuron connectivity calculated using a 100-frame sliding window, with opacity indicating connection strength. Bottom right: Binary-tree representation of maze topology, with the highlighted path dynamically showing the mouse's sequence of choices. Scale bar, 500 μm.

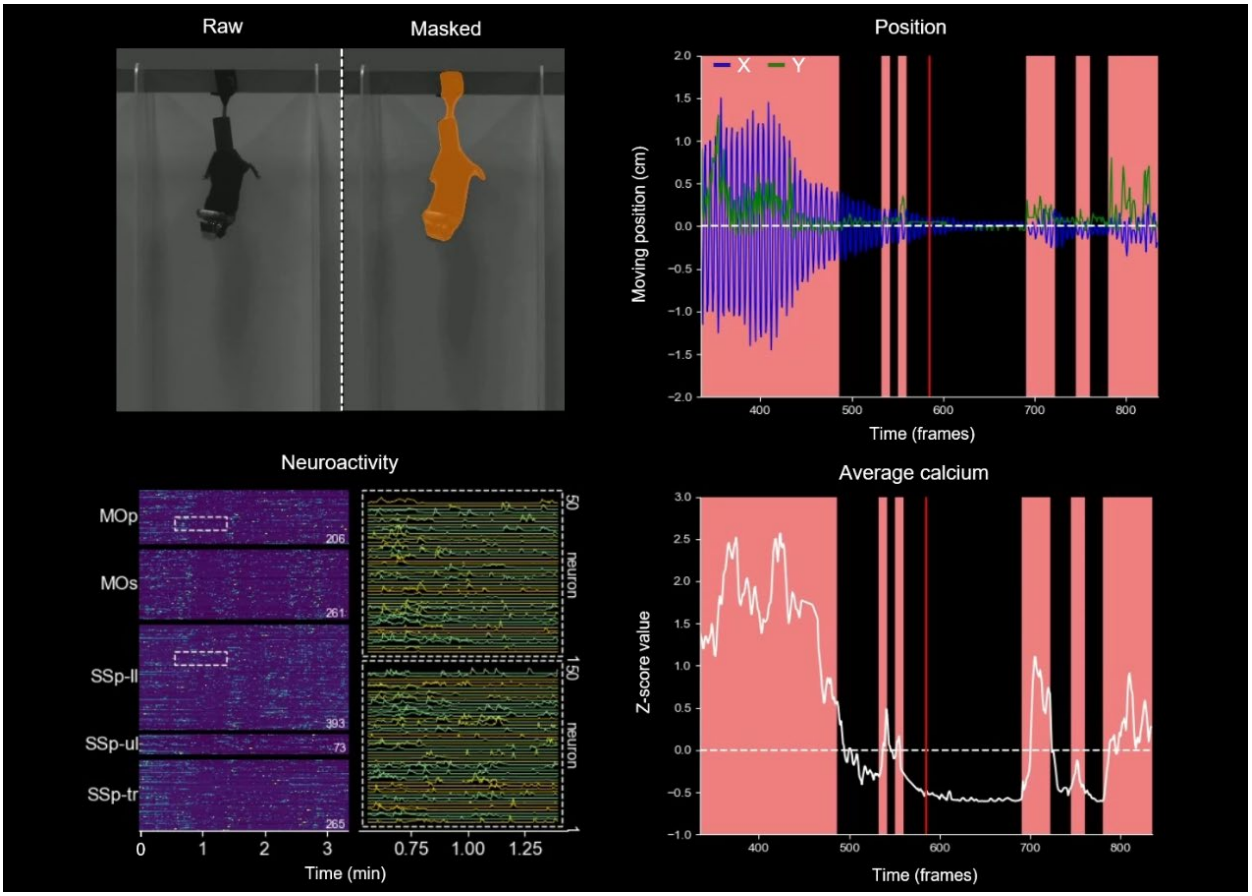
Supplementary Video 10



Neural recording of an animal during forced swimming test (FST) with Airscope.

Top left: Manually annotated locomotor behaviors, categorized into floating, struggling, and swimming (Methods). The white line in the video represents the current time. Bottom left: A mouse equipped with an Airscope performing forced swim test in a cylindrical chamber with a diameter of 20 cm (left). The corresponding segmented mask video generated by SAM2Mice is exhibited (right). Right: Heatmap of neural activity across different brain regions during FST, with traces sampled from two cortical regions presented on the right.

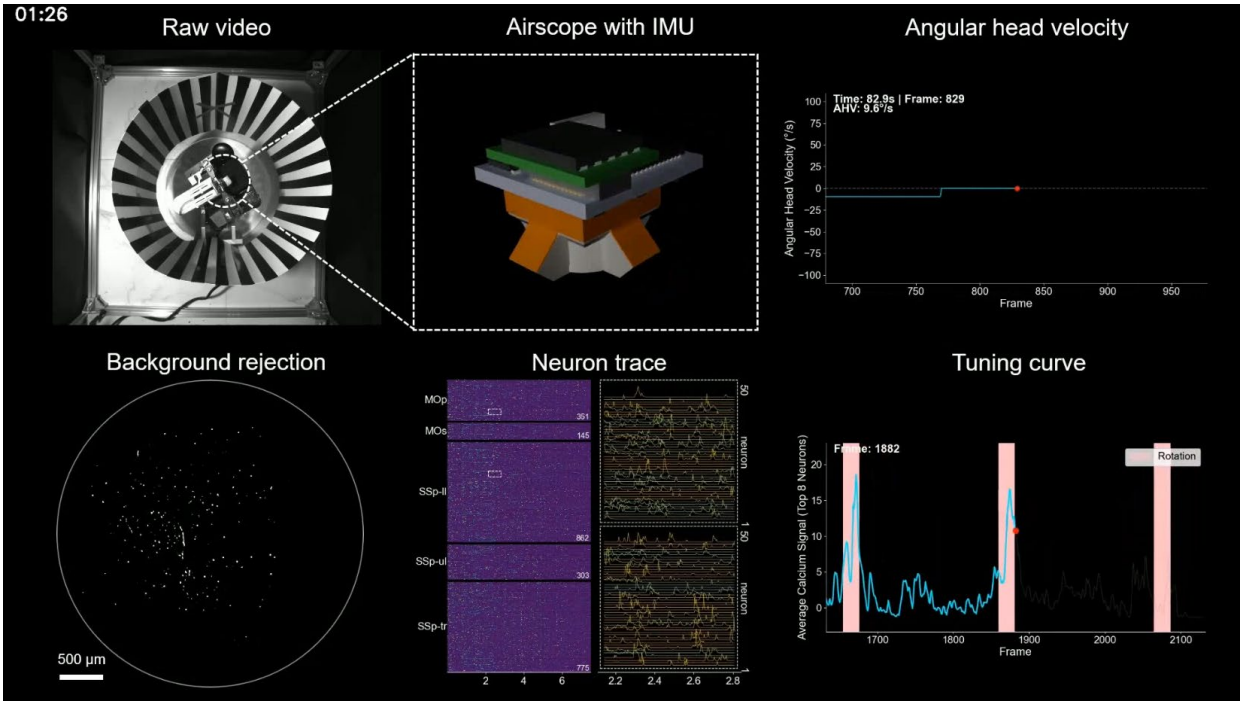
Supplementary Video 11



Neural recording of an animal during tail suspension test (TST) with Airscope.

Top left: Raw and SAM2Mice-masked videos during TST. Top right: X- and Y-axis motion traces, with pink indicating active struggling and black indicating passive periods; the red line marks current time. Bottom left: Multi-region neural activity heatmaps with representative neuronal traces. Bottom right: Mean activity of eight selective neurons over time, showing elevated calcium activity during active struggling and reduced activity during passive periods.

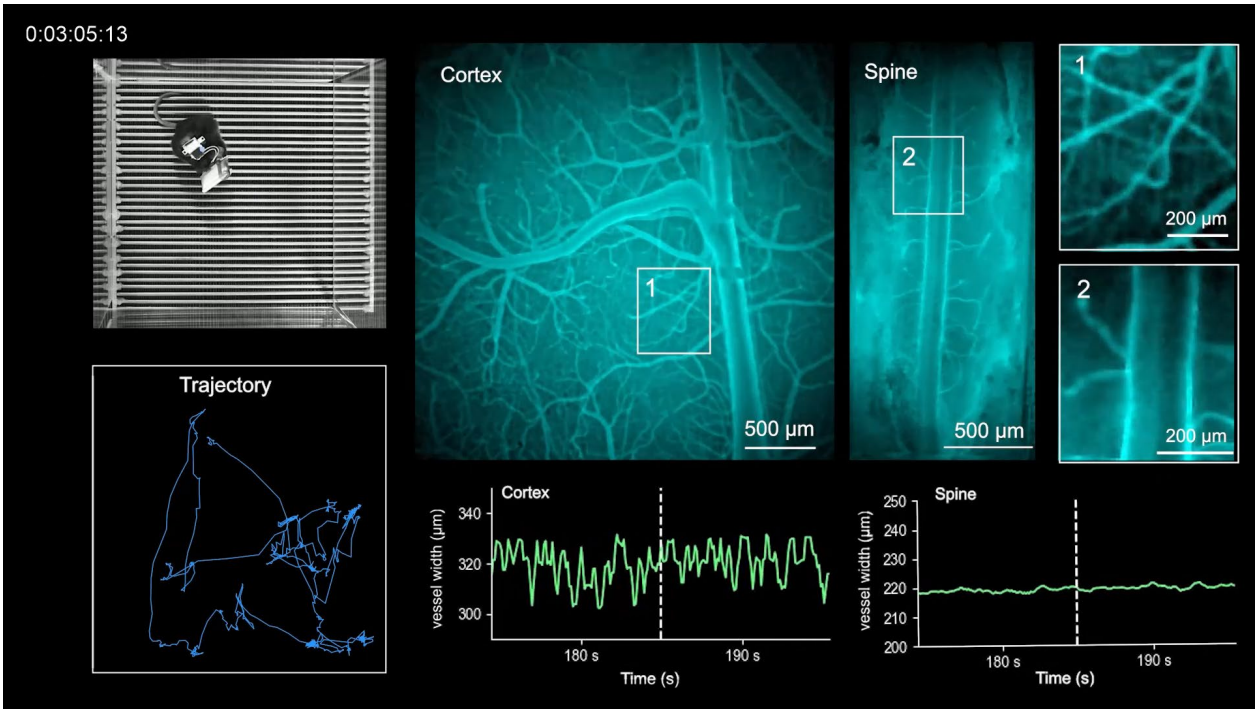
Supplementary Video 12



Neural recording of an animal during head rotation test with Airscope.

Top left and middle: A mouse with Airscope was rotated back and forth at 120° step. Top right: The angular velocities (9.6°/s, 50.4°/s, 91.2°/s) of the rotation test setup. Bottom left: Background removed cortical recordings from Airscope. Bottom middle: Heatmap of neural activity across different brain regions, with traces sampled from two cortical regions presented on the right. Bottom right: Averaged dorsal cortex-wide neuronal activity from n = 8 selective neurons. Pink region indicates animal rotation.

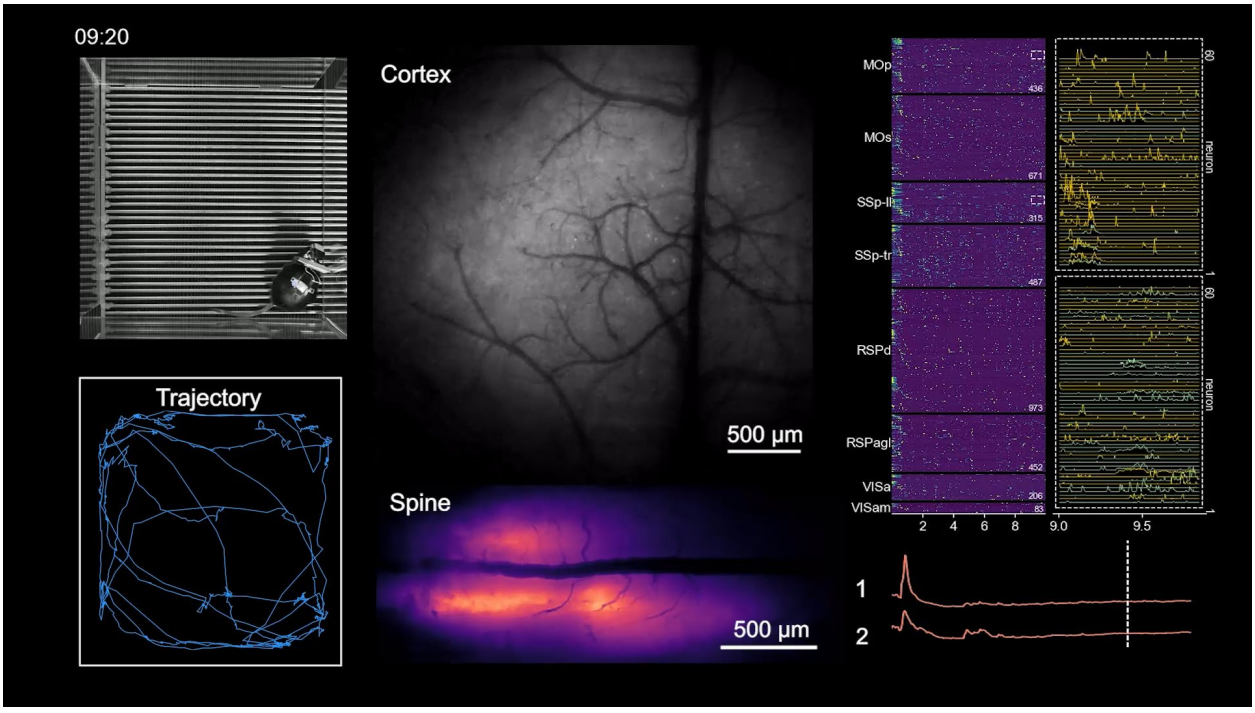
Supplementary Video 13



Simultaneous cortex and spinal cord vascular imaging through Airscope.

Mice equipped with dual Airscopes for concurrent capture of cortical and spinal cord vasculature. Left panels: overhead video (top) and locomotor trajectories. Middle panels: cortical vascular network (top) with corresponding vessel dilation traces (bottom). Right panels: spinal cord vascular network (top) and associated dilation traces (bottom). Scale bar: 500 µm in main panels and 200 µm in zoom-in panels.

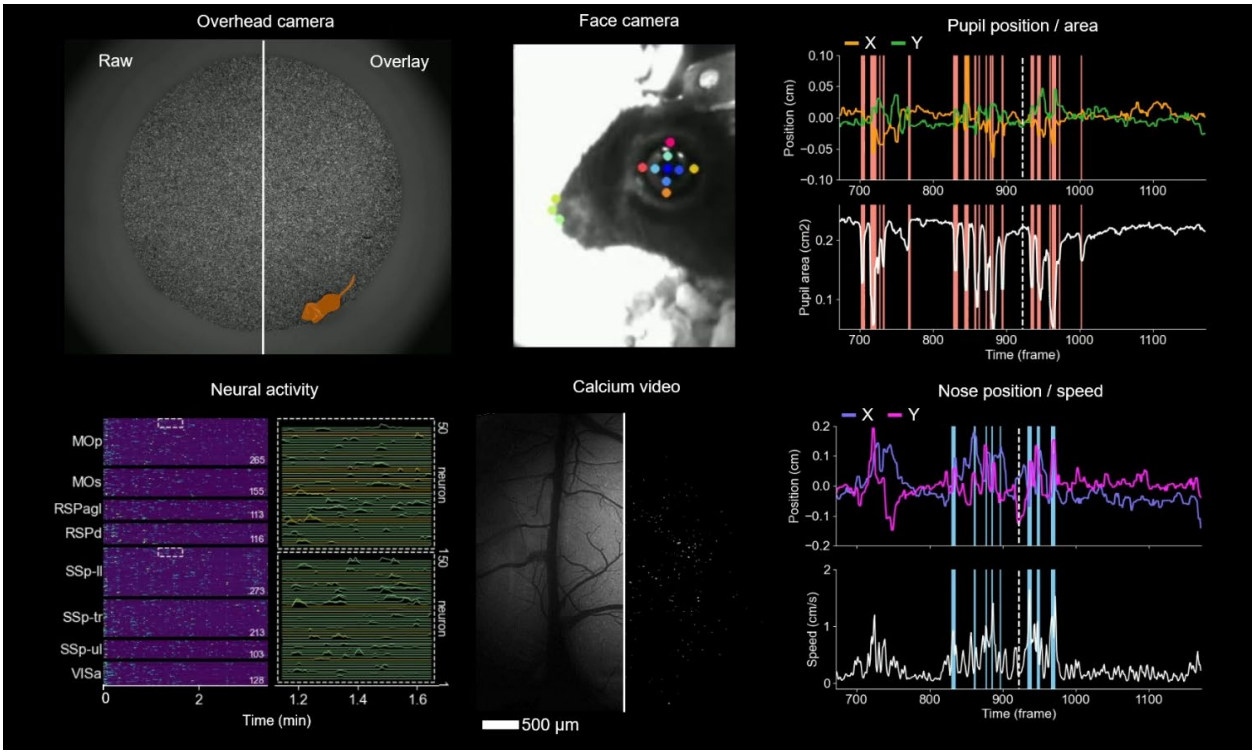
Supplementary Video 14



Simultaneous cortex and spinal cord neural imaging through Airscope.

Mice wearing dual Airscopes for simultaneous recording of cortical neuronal and spinal cord population activity. Left panels: overhead video (top) and locomotor trajectories. Middle panels: cortical calcium activity maps (top) and spinal cord activity video frames (bottom). Right panels: extracted neuronal populations across distinct cortical regions (top) and dynamics of spinal cord functional components (bottom). Scale bar: 500 μm.

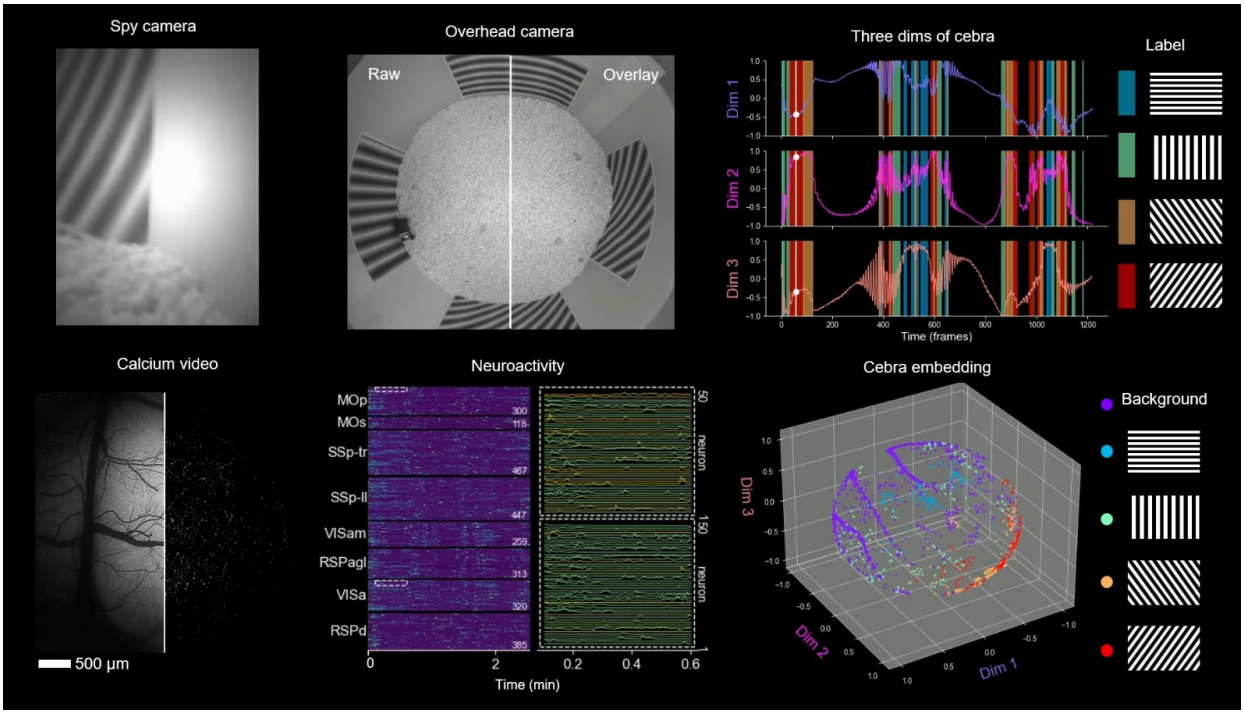
Supplementary Video 15



Integrated recording of neural activity, locomotion, and orofacial dynamics in freely moving mice through Airscope.

Top left: An Airscope-equipped mouse exploring a 60 × 60 cm² open field, shown with raw video and SAM2Mice segmentation. Top middle: Orofacial video with DeepLabCut-tracked pupil, eye, and nose keypoints. Top right: Pupil position and area, with blinks indicated in red. Bottom left: Multi-region neural activity heatmaps with representative traces. Bottom middle: Raw and background-removed calcium imaging. Bottom right: Nose position and locomotion speed, with self-grooming periods indicated in blue. Scale bar, 500 μm.

Supplementary Video 16



Simultaneous neural and first-person view recording of a freely moving animal with Airscope.

Top left: Egocentric visual input recorded by an Airscope-modified head-mounted camera during arena exploration. Top middle: Airscope-equipped mice exploring a 60-cm circular arena with four visual wall cues, shown as raw video and SAM2Mice segmentation. Top right: CEBRA embedding of neural activity into 3D latent space, color-coded by visual cue. Bottom left: Raw and background-removed calcium imaging. Bottom middle: Multi-region neural activity heatmaps with representative traces. Bottom right: Dynamic CEBRA latent trajectories over time, with colors indicating the corresponding visual cues. Scale bar, 500 μm.

References

1. Zhang, Y. *et al.* Rapid detection of neurons in widefield calcium imaging datasets after training with synthetic data. *Nat. Methods* **20**, 747–754 (2023).
2. Pnevmatikakis, E. A. & Giovannucci, A. NoRMCorre: An online algorithm for piecewise rigid motion correction of calcium imaging data. *J. Neurosci. Methods* **291**, 83–94 (2017).
3. Zhou, P. *et al.* Efficient and accurate extraction of in vivo calcium signals from microendoscopic video data. *eLife* **7**, e28728 (2018).
4. *Information on the (previous Version 3) Miniscope platform*, <https://oldwiki.miniscope.org/index.php/Information_on_the_(previous_Version_3)_Miniscope_platform> (2018).
5. *Miniscope V4*, <https://oldwiki.miniscope.org/index.php/Miniscope_V4> (2020).
6. Padilla-Coreano, N. *et al.* Cortical ensembles orchestrate social competition through hypothalamic outputs. *Nature* **603**, 667–671 (2022).
7. Powell, T. R., Fernandes, C. & Schalkwyk, L. C. Depression-Related Behavioral Tests. *Curr. Protoc. Mouse Biol.* **2**, 119–127 (2012).
8. van der Maaten, L. & Hinton, G. Visualizing Data using t-SNE. *J. Mach. Learn. Res.* **9**, 2579–2605 (2008).
9. Keshavarzi, S. *et al.* Multisensory coding of angular head velocity in the retrosplenial cortex. *Neuron* **110**, 532–543.e9 (2022).
10. Dolensek, N., Gehrlach, D. A., Klein, A. S. & Gogolla, N. Facial expressions of emotion states and their neuronal correlates in mice. *Science* **368**, 89–94 (2020).
11. Meyer, A. F., Poort, J., O'Keefe, J., Sahani, M. & Linden, J. F. A Head-Mounted Camera System Integrates Detailed Behavioral Monitoring with Multichannel Electrophysiology in Freely Moving Mice. *Neuron* **100**, 46–60.e7 (2018).
12. Parker, P. R. L., Abe, E. T. T., Leonard, E. S. P., Martins, D. M. & Niell, C. M. Joint coding of visual input and eye/head position in V1 of freely moving mice. *Neuron* **110**, 3897–3906.e5 (2022).
13. Syeda, A. *et al.* Facemap: a framework for modeling neural activity based on orofacial tracking. *Nat. Neurosci.* **27**, 187–195 (2024).
14. Holmgren, C. D. *et al.* Visual pursuit behavior in mice maintains the pursued prey on the retinal region with least optic flow. *eLife* **10**, e70838 (2021).
15. Geng, Y. *et al.* Optical properties of the mouse eye. *Biomed. Opt. Express* **2**, 717–738 (2011).
16. Caron, M. *et al.* Emerging Properties in Self-Supervised Vision Transformers. In *2021 IEEE/CVF International Conference on Computer Vision (ICCV)*, 9650–9660 (2021).
17. Schneider, S., Lee, J. H. & Mathis, M. W. Learnable latent embeddings for joint behavioural and neural analysis. *Nature* **617**, 360–368 (2023).
18. Wang, Q. *et al.* The Allen Mouse Brain Common Coordinate Framework: A 3D Reference Atlas. *Cell* **181**, 936–953.e20 (2020).
19. Hennestad, E., Witoelar, A., Chambers, A. R. & Vervaeke, K. Mapping vestibular and visual contributions to angular head velocity tuning in the cortex. *Cell Rep.* **37**, 110134 (2021).
20. Lauer, J. *et al.* Multi-animal pose estimation, identification and tracking with DeepLabCut. *Nat. Methods* **19**, 496–504 (2022).
21. Ye, S. *et al.* SuperAnimal pretrained pose estimation models for behavioral analysis. *Nat. Commun.* **15**, 5165 (2024).

22. Park, J., Brady, D. J., Zheng, G., Tian, L. & Gao, L. Review of bio-optical imaging systems with a high space-bandwidth product. *Adv. Photonics* **3**, 044001 (2021).
23. Zong, W. *et al.* Fast high-resolution miniature two-photon microscopy for brain imaging in freely behaving mice. *Nat. Methods* **14**, 713–719 (2017).
24. Xue, F. *et al.* Multi-region calcium imaging in freely behaving mice with ultra-compact head-mounted fluorescence microscopes. *Natl Sci. Rev.* **11**, nwad294 (2024).
25. Jacob, A. D. *et al.* A Compact Head-Mounted Endoscope for In Vivo Calcium Imaging in Freely Behaving Mice. *Curr. Protoc. Neurosci.* **84**, e51 (2018).
26. Zong, W. *et al.* Large-scale two-photon calcium imaging in freely moving mice. *Cell* **185**, 1240–1256.e30 (2022).
27. Zhang, Z. *et al.* High-speed neural imaging with multiplexed miniaturized two-photon microscopy. *Cell Rep. Methods* **5**, 101221 (2025).
28. Barbera, G., Liang, B., Zhang, L., Li, Y. & Lin, D. T. A wireless miniScope for deep brain imaging in freely moving mice. *J. Neurosci. Methods* **323**, 56–60 (2019).
29. Klioutchnikov, A. *et al.* Simultaneous two- and three-photon multiplane imaging across cortical layers in freely moving mice. *Nat. Methods* **23**, 1437–1446 (2026).
30. Shuman, T. *et al.* Breakdown of spatial coding and interneuron synchronization in epileptic mice. *Nat. Neurosci.* **23**, 229–238 (2020).
31. de Groot, A. *et al.* NINscope, a versatile miniscope for multi-region circuit investigations. *eLife* **9**, e49987 (2020).
32. Ghosh, K. K. *et al.* Miniaturized integration of a fluorescence microscope. *Nat. Methods* **8**, 871–878 (2011).
33. Cai, D. J. *et al.* A shared neural ensemble links distinct contextual memories encoded close in time. *Nature* **534**, 115–118 (2016).
34. Liberti, W. A., Perkins, L. N., Leman, D. P. & Gardner, T. J. An open source, wireless capable miniature microscope system. *J. Neural Eng.* **14**, 045001 (2017).
35. Bollimunta, A. *et al.* Head-mounted microendoscopic calcium imaging in dorsal premotor cortex of behaving rhesus macaque. *Cell Rep.* **35**, 109239 (2021).
36. Scherrer, J. R., Lynch, G. F., Zhang, J. J. & Fee, M. S. An optical design enabling lightweight and large field-of-view head-mounted microscopes. *Nat. Methods* **20**, 546–549 (2023).
37. Zhao, P. *et al.* MiniXL: An open-source, large field-of-view epifluorescence miniscope enabling single-cell resolution and multi-region imaging in mice. *Sci. Adv.* **11**, eads4995 (2025).
38. Guo, C. *et al.* Miniscope-LFOV: A large-field-of-view, single-cell-resolution, miniature microscope for wired and wire-free imaging of neural dynamics in freely behaving animals. *Sci. Adv.* **9**, eadg3918 (2023).
39. Yartsev, M. M. & Ulanovsky, N. Representation of Three-Dimensional Space in the Hippocampus of Flying Bats. *Science* **340**, 367–372 (2013).
40. Erofeev, A., Antifeev, I., Vinokurov, E., Bezprozvanny, I. & Vlasova, O. An Open-Source Wireless Electrophysiology System for In Vivo Neuronal Activity Recording in the Rodent Brain: 2.0. *Sensors* **23**, 9735 (2023).
41. Wang, Y. *et al.* Cable-free brain imaging for multiple free-moving animals with miniature wireless microscopes. *J. Biomed. Opt.* **28**, 026503 (2023).
42. An, L. *et al.* Three-dimensional surface motion capture of multiple freely moving pigs using MAMMAL. *Nat. Commun.* **14**, 7727 (2023).